AFOSR Deliverables Submission Survey

Thank You

Your report has been submitted. You should receive an email confirmation soon that it is being processed by AFOSR. Please print this page as proof of submission. Thank you.

Principal Investigator Name:	John Brigham
Primary Contact E-mail:	brigham@pitt.edu
Primary Contat Phone Number:	412-624-9047
Grant/Contract Title:	Fundamental Advances in Inverse Mechanics Towards Self-Aware and Intrinsically Adaptable Structural Systems
Grant/Contract Number:	FA9550-11-1-0132
Program Manager:	David Stargel
Report Type:	Final Report
Reporting Period Start Date:	07/01/2011
Reporting Period End Date:	06/30/2014

The objective of this project was to advance computational methods for solving inverse problems related to smart morphable structures that can evaluate their current environment and then adapt accordingly to optimize performance with minimal energy expense. A computational framework was established for the

Abstract: optimal design of morphing structures comprised of active smart materials through locally controllable actuation and activation. The computational optimal design framework for smart material morphing structures was then extended to substantially improve the computational efficiency of the overall solution procedure by replacing the non-gradient-based optimization with gradient-based optimization. In addition, this work sought to explore the use of reduced-order modeling for accurate and efficient inverse problem solution algorithms, and investigated inverse problem solution efficiency in a general sense. The reduced-order modeling component was primary focused on nondestructive evaluation-type inverse problems (e.g., inverse characterization). A computational approach was established to create physics-based reduced-order models for representing the behavior of a boundary value problem (e.g., solid mechanics, heat transfer, etc.) in a generally applicable way, with minimal computational cost, but with accuracy commensurate with traditional finite element analysis methods. Then, an entirely new variation on the use of proper-orthogonal decomposition (POD) bases for inverse material characterization problems through a Gappy POD reconstruction procedure combined with direct inversion was hypothesized, developed, and tested. Lastly, the use of multi-objective optimization, rather than the typically utilized single-objective format, for non-gradient-based optimization-based inverse problem solution strategies was investigated and evaluated. Through simulated examples, the multi-objective approach was shown to maintain a substantially higher diversity in the potential solution set throughout the non-gradient-based optimization in comparison to single-objective approaches.

Distribution Statement: Distribution A - Approved for Public Release

SF298 Form: 85-4f8ef000129c1ba0e50615edf51421b8_Brigham_SF298.pdf

Report Document 81-ccb5493aa35b6121e8987f9a765a8266_Brigham_Final_Report.pdf

1. M. Wang and J.C. Brigham (2014), “A Computational Nondestructive Evaluation Algorithm Combining Self-Evolving Parameterization and Multi-Objective Optimization for Quantitative Damage Characterization,” Journal of Nondestructive Evaluation, 33, 4, December, 547-561.
2. M. Wang and J.C. Brigham, (2014) Invited Paper: “Assessment of Multi-Objective Optimization for Nondestructive Evaluation of Damage in Structural Components,” Journal of Intelligent Material Systems and Structures, 25, 9, June, 1082-1096.
3. S. Wang and J.C. Brigham (2012), “A Computational Framework for the Optimal Design of Morphing Processes in Locally Activated Smart Material

Archival Publications:

Structures," Smart Materials and Structures, 21, 10, October, 105016-105029.
4. S. Wang and J.C. Brigham (2013), "An Adjoint Based Approach for Optimal Design of Morphing SMP," ASME 2013 Conference on Smart Materials, Adaptive Structures and Intelligent Systems, Snowbird, UT, September.
5. Invited Paper, J.C. Brigham, B. Notghi, and S. Wang (2013), "Methods in Computational Inverse Mechanics for the Advancement of Smart Structure Technologies," ASCE 2013 Structures Congress, Pittsburgh, PA, May.
6. S. Wang and J.C. Brigham (2012), "An Efficient Computational Inverse Approach for Optimal Design of Localized Activation and Actuation for Morphing SMP Structures," ASME 2012 Conference on Smart Materials, Adaptive Structures and Intelligent Systems, Stone Mountain, GA, September.
7. M. Wang and J.C. Brigham (2012), "Evaluation of Damage in a Continuum through a Multi-Objective Optimization Inverse Approach," ASME 2012 Conference on Smart Materials, Adaptive Structures and Intelligent Systems, Stone Mountain, GA, September.
8. M. Ahmadpoor and J.C. Brigham (2013), "An Approach for Adaptive Generation of Reduced-Order Models for Applications in Nondestructive Evalution," Conference of the Engineering Mechanics Institute, Evanston, IL, August.
9. M. Wang and J.C. Brigham (2013), "An Adaptive Damage Characterization Strategy Utilizing Multi-Objective Optimization," Conference of the Engineering Mechanics Institute, Evanston, IL, August.
10. S. Wang and J.C. Brigham (2013), "Computationally Efficient Optimal Design of Localized Activation and Actuation for Morphing SMP Structures Using the Adjoint Method," 12th US National Congress on Computational Mechanics, Raleigh, NC, July.
11. M. Ahmadpoor and J.C. Brigham (2013), "An Adaptive Approach for Generation of Reduced-Order Models for Computational Inverse Mechanics Strategies," 12th US National Congress on Computational Mechanics, Raleigh, NC, July.
12. S. Wang and J.C. Brigham (2012), "An Efficient Computational Inverse Approach for Optimal Design of Localized Activation and Actuation for Morphing SMP Structures," International Conference on Inverse Problems and Related Topics 2012, Nanjing, Jiangsu, China, October.
13. S. Wang and J.C. Brigham (2012), "A Computational Approach for Optimal Design of Smart Material Morphing Structures Through Adaptable Activation," 2012 Joint Conference of the Engineering Mechanics Institute and the 11th ASCE Joint Specialty Conference on Probabilistic Mechanics and Structural Reliability,

	Notre Dame, IN, June. 14. M. Wang and J.C. Brigham (2012), "A Multi-Objective Optimization-Based Approach to Nondestructive Evaluation of Damage in a Continuum," 2012 Joint Conference of the Engineering Mechanics Institute and the 11th ASCE Joint Specialty Conference on Probabilistic Mechanics and Structural Reliability, Notre Dame, IN, June.
Changes in Research objectives:	None
Change in AFOSR Program Manager, if any:	None
Extensions granted or milestones slipped, if any:	None

100%

Accomplishments/New Findings:

- A computational framework was established for the optimal design of morphing structures comprised of active smart materials through locally controllable actuation and activation. The framework combined finite element analysis to predict the morphing process for a given set of activation and actuation parameters with nonlinear optimization to identify the optimal set of those parameters. For context the framework was developed for the specific application of morphing structures comprised of thermally responsive polymers, and therefore the activation was applied thermal stimulus. The framework was capable of considering linear transient heat transfer coupled with quasi-static solid mechanics. Specific targets of the design process that could be considered including the desired motion or kinematic of the structure as well as the energy and time required to complete the morphing process.
- The initial incarnation of the computational optimal design framework for smart material morphing structures utilized non-gradient-based optimization to ensure that the design solution was near to the global optimum regardless of computational expense. This framework was numerically evaluated through simulated case studies. The framework was shown to be capable of identifying design parameters, including activation and actuation locations and sequencing, to produce substantial savings in terms of total energy cost and more accurately achieve a desired shape change in comparison to standard intuitive designs.
- The computational optimal design framework for smart material morphing structures was extended to substantially improve the computational efficiency of the overall solution procedure by replacing the non-gradient-based optimization with gradient-based optimization. Furthermore, to even further improve the computational efficiency an adjoint approach was formulated and implemented to calculate the gradient of the design objectives with respect to the morphing system activation and actuation parameters that only required the equivalent of two finite element analyses per iteration. Again, the design procedure with gradient-based optimization was shown to be capable of identifying design parameters, including activation and actuation locations and sequencing, to produce substantial savings in terms of total energy cost and more accurately achieve a desired shape change in comparison to standard intuitive designs. Furthermore, although the design solutions were less optimal than those that could be obtained with non-gradient-based optimization, the computational cost of the gradient-based approach was multiple orders of magnitude less than that of the gradient-based optimization.
- A computational approach was established to create physics-based reduced-order models (ROM) for representing the behavior of a boundary value problem (e.g., solid mechanics, heat transfer, etc.) in a generally applicable way, with minimal computational cost, but with accuracy commensurate with traditional finite element analysis methods. The approach utilized the reduced-basis ROM technique and was established in the context of inverse problem applications, such that the accuracy of the ROM is maximized over a range of system parameters that will ultimately be solved for through an inverse problem solution strategy. The ROM creation approach was tested with example nondestructive evaluation

problems and was shown to provide a sufficiently accurate representation of the system physics to be utilized in an inverse problem solution technique, and required only a fraction of the cost of a standard finite element analysis method.

- An entirely new variation on the use of proper-orthogonal decomposition (POD) bases for inverse material characterization problems was hypothesized, developed, and tested. This new variation creates a POD basis from a previously generated or observed set of system response fields for the system to be characterized as is typical. However, rather than use the basis to recreate a reduced-order model, the basis is used with the Gappy POD machine learning technique to create a tool that predicts a full-field response from partial field measurements (as would be available from nondestructive testing techniques). Then, the full-field response is utilized with a direct inversion strategy to predict the inverse characterization solution. The approach was shown through simulated nondestructive evaluation problems to require a fraction of the cost of typical iterative inverse problem solution techniques, to maintain general applicable, and to still provide accurate inverse solution estimates.
- The use of multi-objective optimization, rather than the typically utilized single-objective format, for non-gradient-based optimization-based inverse problem solution strategies was investigated and evaluated. Through simulated examples, the multi-objective approach was shown to maintain a substantially higher diversity in the potential solution set throughout the non-gradient-based optimization in comparison to single-objective approaches. This increase in diversity was shown to substantially improve the efficiency of the optimization-based solution strategy as well as the consistency and accuracy of the final solution estimate. In addition, a strategy was developed to utilize this solution diversity throughout the inverse problem solution procedure to adaptive modify the parameterization of the unknown field of the inverse problem, thereby further increasing the accuracy and efficiency of the inverse problem solution estimation procedure.

SUMMARY

A strategy to obtain maximally efficient and accurate morphing structures composed of active materials such as shape memory polymers (SMP) through synchronization of adaptable and localized activation and actuation was established and numerically tested. A computational inverse mechanics framework was created that combines a computational representation of the SMP thermo-mechanical behavior with a nonlinear optimization algorithm to determine location, magnitude and sequencing of the activation and actuation to obtain a desired shape change subject to design objectives such and prevention of damage. The concept of localized activation along with the optimal design strategy were shown to be able to produce far more energy efficient morphing structures and more accurately reach the desired shape change in comparison to traditional methods that require complete structural activation prior to actuation.

The computational strategy for estimation of the optimal parameters relating to the distribution and sequencing of activation and actuation for a morphing smart material structure or structural component to efficiently and effectively achieve a desired morphing function was extended to substantially increase computational efficiency. In particular, a formulation of the adjoint method was developed to be utilized to estimate the gradient of the objective function(s) with respect to the activation and actuation parameters with minimal computational expense within a gradient-based optimization strategy, which then provides an optimization process that is substantially computationally efficient overall. Overall, the computational optimal design approach with the adjoint method was shown to provide the capability to efficiently identify activation and actuation parameters to achieve desired morphing capabilities. Furthermore, the computational approach was shown to be capable of determining energy-efficient design solutions for a diverse set of target shape changes with fixed instrumentation, providing the potential for substantial functionality beyond what could be expected through traditional empirical design strategies.

A generally applicable algorithm for adaptive generation of data ensembles to efficiently create accurate computational mechanics reduced-order models (ROM) for use in computational approaches to approximate inverse problem solutions was developed and numerically evaluated. The ROM approach considered was based on identifying the optimal low-dimensional basis to be used within a Galerkin weak-form finite element method to provide substantially reduced computational cost while maintaining accuracy relative to that of a (traditional) full-order finite element model. The core hypothesis of the algorithm presented is that maximizing the diversity, as defined in a measurable sense, of the full-order models used to create the ROM will maximize the accuracy of the ROM over a range of input system parameters. The adaptive snapshot generation algorithm was shown to produce ROMs that can accurately estimate response fields over a wide range of input parameters, and which are substantially more accurate than ROMs created from randomly generated snapshot sets. Moreover, the accurate generalization of the adaptively generated ROMs was shown to be sufficient to consistently produce accurate inverse characterization solution estimates with a fraction of the computational expense that would be required to do so with full-order analyses.

A new and unique approach for computationally efficient inverse material characterization from partial-field response measurements that combines the Gappy proper orthogonal decomposition (POD) machine learning technique with a physics-based direct inversion strategy was created and evaluated. Gappy POD is used to derive a data reconstruction tool from a set of potential

system response fields that are generated from available *a priori* information regarding the potential distribution of the unknown material properties. Then, the Gappy POD technique is applied to reconstruct the full spatial distribution of the system response from whatever portion of the response field has been measured with the chosen system testing method. Lastly, a direct inversion strategy is presented that is derived from the equations governing the system response (i.e., physics of the system), which utilizes the full-field response reconstructed by Gappy POD to produce an estimate of the spatial distribution of the unknown material properties. The inversion procedure was shown to have the capability to efficiently provide accurate estimates to material property distributions from partial-field response measurements. The direct inversion with Gappy POD response estimation was also shown to be substantially tolerant to noise in comparison to the direct inversion given measured full-field response.

A multi-objective optimization-based computational approach to nondestructive evaluation of material properties was numerically evaluated. The multi-objective approach provides a substantial improvement in the capabilities to traverse the optimization search space to minimize the measurement error and produce accurate damage estimates. In addition, a novel self-evolving parameterization approach for nondestructive evaluation was developed and numerically evaluated. The adaptive approach utilizes the substantial solution diversity that is uniquely provided by multi-objective optimization to iteratively build up the parameterization and accurately characterize all property changes with the minimum dimensional parameterization. The nondestructive evaluation approach with self-evolving parameterization was shown to provide an accurate and efficient process for the solution of inverse characterization problems.

Optimal Design of Locally Activated Smart Material Morphing Structures:

Figure 1 illustrates the general form of the morphing structure design (and analogously control) problems considered. In this concept, the morphing process begins with some portion of the domain heated with a controllable transient temperature distribution and/or surface heat flux ($T^A(\vec{x},t)$ or $q^A(\vec{x},t)$). Once a sufficient portion of the structure is softened through activation, mechanical actuation begins through controlled transient displacement and/or force ($\vec{u}^A(\vec{x},t)$ or $\vec{\tau}^A(\vec{x},t)$) to deform the structure into a desired shape. Therefore, the design/control problem to identify the activation and actuation distributions to achieve the desired shape change can be cast in a general way in the form of the following constrained optimization problem:

$$Minimize: \begin{cases} \parallel s^{target} - s^{approx}(T^A, q^A, \vec{u}^A, \vec{\tau}^A) \parallel_{\Omega,t_F} \\ J_T(T^A, q^A, \vec{u}^A, \vec{\tau}^A) \\ J_W(T^A, q^A, \vec{u}^A, \vec{\tau}^A) \\ t_F(T^A, q^A, \vec{u}^A, \vec{\tau}^A) \\ w(T^A, q^A, \vec{u}^A, \vec{\tau}^A) \end{cases} \tag{1}$$

$$Subject\ to: \begin{cases} \tilde{\sigma}(\boldsymbol{\sigma}(\vec{x},t;T^A, q^A, \vec{u}^A, \vec{\tau}^A)) < \sigma^{damage}, \quad \forall \vec{x} \in \Omega, \quad t \in [0,t_F] \\ T(\vec{x},t;T^A, q^A, \vec{u}^A, \vec{\tau}^A) < T^{damage}, \quad \forall \vec{x} \in \Omega, \quad t \in [0,t_F] \end{cases} \tag{2}$$

where $\vec{x}$ is the spatial position vector, t is the time, Ω is the spatial domain of the structure, t_F is the total time of the morphing process, $\|\cdot\|_{\Omega,t_F}$ is the metric norm with respect to the spatial domain and time, s^{target} is the desired shape change, s^{approx} is the approximate expected shape change given the design parameters predicted by a numerical representation of the structure, J_T and J_W are the total thermal energy and mechanical work, respectively, predicted by the numerical representation to perform the morph, w represents additional design objectives that may be desired, $\boldsymbol{\sigma}$ and T are the approximate expected internal stress tensor and internal temperature, respectively, predicted by the numerical representation throughout the structure during the morphing process, $\tilde{\sigma}(\cdot)$ is a suitable scalar stress transform (e.g., von Mises criterion), and σ^{damage} and T^{damage} are the stress and temperature limits, respectively, to avoid damaging the material. A framework was built to solve the constrained optimization problem (Eqns. (1) - (2)) through a computational inverse problem solution approach that combines a numerical representation of the morphing system (i.e., forward problem) and a nonlinear optimization strategy to identify the parameters that minimize the desired objectives while satisfying the required constraints.

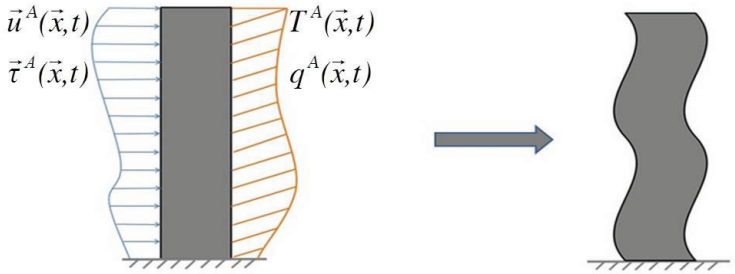

Figure 1: Schematic of the morphing structure design problem in which the applied activation (T^A or q^A) and actuation ($\vec{u}^A$ or $\vec{\tau}^A$) are to be determined to achieve a desired shape change.

Two optimization approaches were investigated for the solution of this (now PDE-constrained) optimization problem. The first portion of the investigation (i.e., the proof-of-concept) used a genetic algorithm, a stochastic global search algorithm that mimics the process of evolution in nature [1, 2]. Genetic algorithms (GAs) are heuristic optimization approaches that generally rely on three main operations to evolve a population of potential solutions to the optimization problem parameters: survival, reproduction, and mutation. GAs have seen substantial use in recent years due to their ease of implementation (e.g., there is no need for complicated gradient calculations), global search capabilities, and simplicity of parallelization. However, GAs may not be ideal for many applications in computational inverse mechanics due to the large number of function evaluations (i.e., numerical simulations) that are typically required to converge to an optimal solution. To create a substantially more realistically applicable framework, the second portion of the work utilized gradient-based optimization, particularly relying on the adjoint approach to expedite gradient calculations. A quasi-Newton gradient-based algorithm, the BFGS interior point algorithm [3, 4, 5], was chosen for this purpose.

To present the adjoint formulation developed and implemented, consider the following specific example form of the optimal design/control objective functional:

$$f(\vec{p}) = J(\vec{p}) + C \cdot S(\vec{p}) \tag{3}$$

where $\vec{p}$ is the vector of unknown design parameters to be determined through the optimization (i.e., activation and actuation parameters) and C is the scalar weighting constant (note that the specific value of the weighting constant allows emphasis of the optimization effort to be placed on a specific objective, energy or shape, depending on the relative importance for a particular application). The total energy of the morphing process ($J = J_T + J_W$) can be defined with:

$$J_T = \int_t \int_\Omega \rho c[T(\vec{x}, t) - T_0]\delta(t - t_F) d\vec{x} dt \tag{4}$$

and

$$J_W = \int_t \int_\Gamma \boldsymbol{\sigma}(\vec{x}, t) \cdot \vec{n}(\vec{x}) \cdot \vec{u}(\vec{x}, t) d\vec{x} dt, \tag{5}$$

where δ is the Dirac delta function, and the morphing error could be defined as:

$$S = \int_t \int_\Omega \sum_{m=1}^{M} \left[\vec{u}(\vec{x}, t) - \vec{u}^{target}(\vec{x}, t)\right]^2 \delta(\vec{x} - \vec{x}_m^*)\delta(t - t_F) d\vec{x} dt, \tag{6}$$

where $\vec{u}$ and $\vec{u}^{target}$ are the predicted and desired (i.e., target) displacement fields, respectively, $\{\vec{x}_m^*\}_{m=1}^M$ is the set of M discrete spatial locations where the target displacement is desired to be achieved by the morph, and t_F is the time at the completion of the morphing process. For simplicity of illustration, the activation process can be assumed to occurred entirely through a temperature-dependent Young's, and the behavior of the structures was assumed to be defined by linear transient heat transfer and linear elastic quasi-static solid mechanics. Therefore, the morphing process of a

smart material structure could be represented by the following initial boundary value problem:

$$
\begin{array}{ll}
k\nabla^2 T(\vec{x},t) = \rho c \frac{\partial T(\vec{x},t)}{\partial t}, & \forall\ \vec{x} \in \Omega,\ t \in [0, t_F], \\
\nabla \cdot \boldsymbol{\sigma}(\vec{x},t) = \vec{0}, & \forall\ \vec{x} \in \Omega,\ t \in [0, t_F], \\
T(\vec{x},0) = T_0, & \forall\ \vec{x} \in \Omega,\ t = 0, \\
T(\vec{x},t) = T^A(\vec{x},t), & \forall\ \vec{x} \in \Gamma_T,\ t \in [0, t_F], \\
-k\nabla T(\vec{x},t) \cdot \vec{n}(\vec{x}) = q^A, & \forall\ \vec{x} \in \Gamma_q,\ t \in [0, t_F], \\
\vec{u}(\vec{x},t) = \vec{u}^A(\vec{x},t), & \forall\ \vec{x} \in \Gamma_U,\ t \in [0, t_F], \\
\boldsymbol{\sigma}(\vec{x},t) \cdot \vec{n}(\vec{x}) = \vec{\tau}^A(\vec{x},t), & \forall\ \vec{x} \in \Gamma_{\vec{\tau}},\ t \in [0, t_F], \\
\boldsymbol{\sigma}(\vec{x},t) = \boldsymbol{C^{IV}}(E(T),\nu) : \boldsymbol{\epsilon}(\vec{x},t), & \forall\ \vec{x} \in \Omega,\ t \in [0, t_F], \\
\boldsymbol{\epsilon}(\vec{x},t) = \frac{1}{2}[\nabla \vec{u}(\vec{x},t) + \nabla \vec{u}(\vec{x},t)^T], & \forall\ \vec{x} \in \Omega,\ t \in [0, t_F],
\end{array}
\tag{7}
$$

where k is the thermal conductivity, ρ is the mass density, c is the specific heat, $\boldsymbol{\sigma}$ is the Cauchy stress tensor, $\boldsymbol{\epsilon}$ is the small strain tensor, $\boldsymbol{C^{IV}}$ is the fourth order elastic stiffness tensor, E is the Young's modulus, ν is the Poisson's ratio, $\vec{u}$ is the displacement vector, Ω is the spatial domain, Γ is the domain boundary, $\vec{n}$ is the unit outward normal vector on the boundary. Γ_T is the portion of the domain boundary where the temperature is specified, Γ_q is the portion of the domain boundary where the heat flux is specified, Γ_U is the portion of the domain boundary where the displacement is specified, and $\Gamma_{\vec{\tau}}$ is the portion of the domain boundary where the traction is specified. Following the procedure for the adjoint method [6], for the above forward problem the adjoint problem for the Lagrange multipliers (λ and $\vec{\varphi}$) can be written as:

$$
\begin{array}{ll}
k \bigtriangledown^2 \lambda(\vec{x},t) + \rho c \frac{\partial \lambda(\vec{x},t)}{\partial t} - \frac{1}{E}\frac{\partial E}{\partial T}(\bigtriangledown \vec{\varphi}) : \boldsymbol{\sigma}_{\vec{u}} = 0, & \forall\ \vec{x} \in \Omega,\ t \in [0, t_F], \\
\bigtriangledown \cdot \boldsymbol{\sigma}_{\vec{\varphi}}(\vec{x},t) + C \sum_{m=1}^{M} 2[\vec{u} - \vec{u}^{target}]\delta(\vec{x} - \vec{x}_m^*)\delta(t - t_F) = \vec{0}, & \forall\ \vec{x} \in \Omega,\ t \in [0, t_F], \\
\lambda(\vec{x}, t_F) = 0, & \forall\ \vec{x} \in \Omega,\ t = t_F, \\
\lambda(\vec{x},t) = 0, & \forall\ \vec{x} \in \Gamma_T,\ t \in [0, t_F], \\
-k \bigtriangledown \lambda(\vec{x},t) \cdot \vec{n}(\vec{x}) = 0, & \forall\ \vec{x} \in \Gamma_q,\ t \in [0, t_F], \\
\vec{\varphi}(\vec{x},t) = -\vec{u}^A(\vec{x},t), & \forall\ \vec{x} \in \Gamma_U,\ t \in [0, t_F], \\
\boldsymbol{\sigma}_{\vec{\varphi}}(\vec{x},t) \cdot \vec{n}(\vec{x}) - \vec{\tau}^A \delta(t - t_F) + \frac{\partial \vec{\tau}^A}{\partial t} = \vec{0}, & \forall\ \vec{x} \in \Gamma_{\vec{\tau}},\ t \in [0, t_F],
\end{array}
\tag{8}
$$

Then, the gradient of the objective function can be calculated as:

$$
\begin{array}{l}
\frac{\mathrm{d}L}{\mathrm{d}p_j} = \int_t \int_{\Gamma_T} (-k \bigtriangledown \lambda \cdot \vec{n}) \frac{\partial T^A}{\partial p_j} d\vec{x} dt - \int_t \int_{\Gamma_q} (\lambda \frac{\partial q^A}{\partial p_j}) d\vec{x} dt \\
+ \int_t \int_{\Gamma_{\vec{\tau}}} \left(\vec{\varphi} + \vec{u}^A \right) \frac{\partial \vec{\tau}^A}{\partial p_j} d\vec{x} dt + \int_t \int_{\Gamma_U} (-\boldsymbol{\sigma}_{\vec{\varphi}} \cdot \vec{n} \cdot \frac{\partial \vec{u}^A}{\partial p_j} + \boldsymbol{\sigma}_{\vec{u}} \cdot \vec{n} \cdot \frac{\partial \vec{u}^A}{\partial p_j}) d\vec{x} dt,
\end{array}
\tag{9}
$$

where

$$
\boldsymbol{\sigma}_{\vec{u}} = \frac{E}{2(1+\nu)}[\nabla \vec{u} + \nabla(\vec{u})^T] + \frac{E}{(1+\nu)(1-2\nu)}(\nabla \cdot \vec{u})\mathbf{I}, \tag{10}
$$

$$
\boldsymbol{\sigma}_{\vec{\varphi}} = \frac{E}{2(1+\nu)}[\nabla \vec{\varphi} + \nabla(\vec{\varphi})^T] + \frac{E}{(1+\nu)(1-2\nu)}(\nabla \cdot \vec{\varphi})\mathbf{I}, \tag{11}
$$

and $\mathbf{I}$ is the identity tensor. The algorithm for the calculation of the gradient using the adjoint method can be summarized as follows:

(1) Solve the forward initial boundary value problem (Eqns. (7)) to obtain the displacement field $\vec{u}$ and the temperature field T.
(2) Solve the adjoint initial boundary value problem (Eqns. (8)) to obtain the Lagrange multipliers λ and $\vec{\varphi}$.
(3) Substitute $\vec{u}$, T, λ and $\vec{\varphi}$ into Eqn. (9) to compute the gradient of the objective function.

For this work, the forward initial boundary value problem and the adjoint problem were solved using the traditional Galerkin finite element method.

To test the inherent benefits and challenges of the developed computational approach, numerical investigations were performed with example design applications from concepts of morphing skeletal structural components (i.e., framing and connecting elements). A smart link concept with direct shape control was tested to verify the computational framework, as well as to compare the efficiency and effectiveness of the computational approach using the adjoint method with the non-gradient-based genetic algorithm approach. Then, an example of a morphing structural backbone with substantially increased complexity of design parameters and objectives was considered. As shown in Figure 2, the smart link consisted of a $20mm \times 5mm \times 1mm$ homogeneous rectangular prism composed of thermally responsive SMP. The morphing procedure considered involved first heating the structure in its cast configuration to initiate the activation process. After some time of purely heating, actuation would be applied to deform the structure into the desired shape. As such, the total time to perform the structural morphing, t_F, was simply the summation of the purely heating time prior to actuation, t_D, and the actuation time, t_M. A schematic of the structural backbone considered for the second example is shown in Figure 3. The structure was taken to be a homogeneous half-circular prism with a $150mm$ outer radius composed of thermally responsive SMP. The morphing procedure applied followed a similar sequencing pattern as the first example. However, to provide greater degrees of freedom for the design/control of the morphing system, several more heating pads and actuators were employed in this case compared to the first example, with a total of nine pairs of approximately 45mm long heating pads and eight approximately 15mm long actuation regions, all equally spaced along the surface of the structure. Additionally, the operation of the structure and the design/control objectives were assumed to be symmetric with respect to the horizontal access. Thus, only the top half to the structure needed to be analyzed and the morphing process of the structure was defined by 10 independent heating pads and four

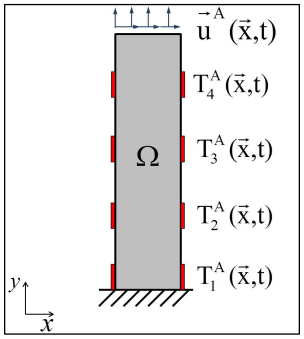

Figure 2: Schematic of the smart link design concept.

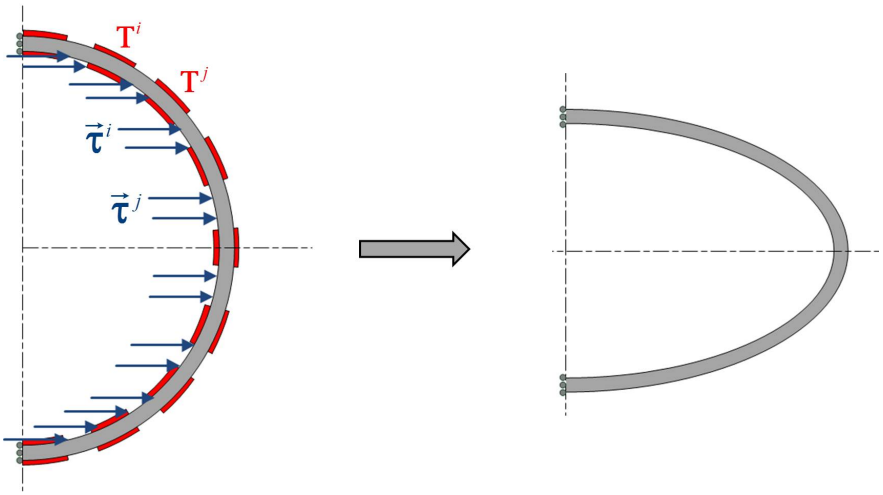

Figure 3: Schematic of the Morphing Structural Backbone Design Concept.

Table 1: Control, optimized design parameters from Genetic Algorithm optimization (GA Opt), optimized design parameters from quasi-Newton gradient-based optimization using the adjoint method (Adjoint Opt), resulting energy consumption to perform the morph, and the percent difference (%Diff) with respect to the control design for the Smart Link example ($mJ = 10^{-3} Joule$).

Design Case	t_T^1 (s)	t_T^2 (s)	t_T^3 (s)	t_T^4 (s)	J_T (mJ)	J_W (mJ)	J (mJ)
Control	80.0	80.0	80.0	80.0	14037.5	10.4	14047.9
GA Opt	44.4	42.5	41.5	69.3	9231.2	83.2	9314.5
%Diff	-44.5	-46.9	-48.2	-13.3	-34.2	+704.0	-33.7
Adjoint Opt	51.0	57.3	65.6	66.7	10833.9	86.7	10920.6
%Diff	-36.2	-28.4	-18.0	-16.6	-22.8	+737.1	-22.3

actuators (note that the heating pad pairs were not linked in this example as was the case in the first example).

Table 1 shows a set of "control" design parameters, the optimized design parameters from the GA optimization, and the optimized design parameters from the gradient-based optimization using the adjoint method, along with the corresponding activation thermal energy (J_T), actuation mechanical work (J_W), and total energy (J), and the percent difference for these energies with respect to the control design for the smart link example. The GA results represent an approximation of the best possible results that could obtained from the computational design procedure, yielding an energy savings of more than 30% with respect to the control design, but required an extensive computational cost, on the order of 10^4 function evaluations, to achieve convergence. Alternatively, the gradient-based optimization results were able to yield less energy savings than the GA, but still a substantial amount at over 20% with respect to the control design, but required two orders of magnitude less function evaluations, on the order of 10^2, than the GA to achieve convergence (even

with the 10 runs with different initial parameter sets). Furthermore, it is often the case for design or control problems such as this that an approximation of the global minimum is unnecessary, and a local solution would be sufficient. In such instances, the substantial improvement in computational savings provided by the gradient-based approach with the adjoint method would likely outweigh the loss in global search capabilities. Table 2 shows three morphing target shapes considered (elliptic, square, and step-type), the optimal design solutions for each target shape, and the corresponding temperature distributions at the initiation of morphing, final stress distributions, and final deformed shapes for the morphing structural backbone example. All of the optimal design solutions can be seen to have produced recognizable approximations to the target shapes, which is particularly significant considering that each of the three shapes is considerably different from one another and yet the morphing mechanism (i.e., activators and actuators) used to achieve the shapes is identical. However, there was a degradation in the morphing accuracy as the complexity of the target shape change increased, which is not necessarily unexpected. This morphing accuracy can be seen quantitatively through the relative difference between the optimized morphing error (S_{opt}) and the morphing error for the starting shape (S_0), which was approximately 90% for the elliptic shape, 40% for the square shape, and 10% for the step-type shape. The target step-type shape was clearly the most challenging to achieve, both intuitively and based on the optimization results, particularly since it was the only shape that required a change from convex to concave. Furthermore, the results would imply that to better achieve a target shape similar to the step-type the starting shape or the morphing mechanisms (i.e., activators and actuators) would need further modification. However, overall, the multiple localized activations and actuations showed the capability to accurately and efficiently achieve a diverse set of shape changes with a fixed set of morphing mechanisms, and the computational approach was particularly well-suited to facilitate the implementation, particularly where intuitive design approaches would be infeasible.

Table 2: Optimized (Opt) design solutions (temperature distribution and final stress distribution) with respect to three different target shapes (ellipse, square and step-type) for the Morphing Structural Backbone example.

Target Shape	Temperature Distribution (K)	Stress Distribution (Pa)
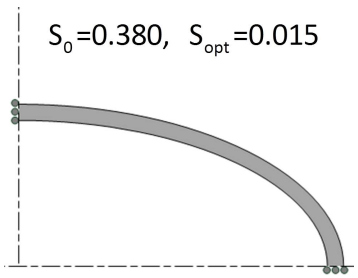	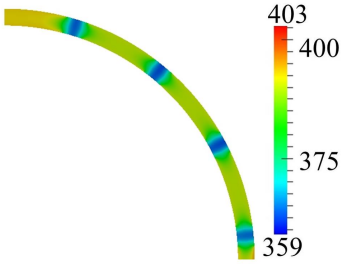	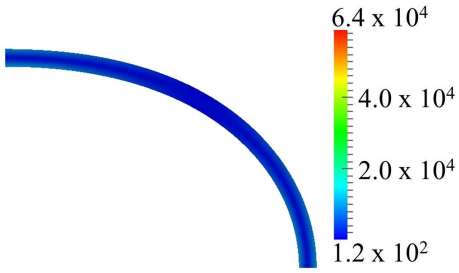
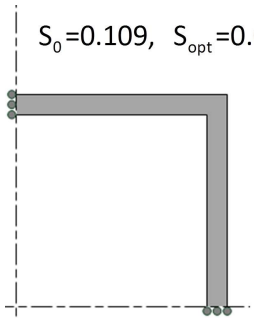	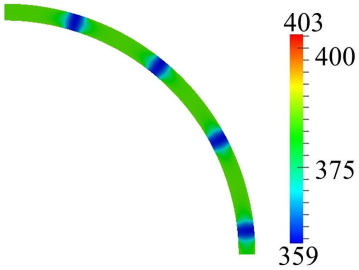	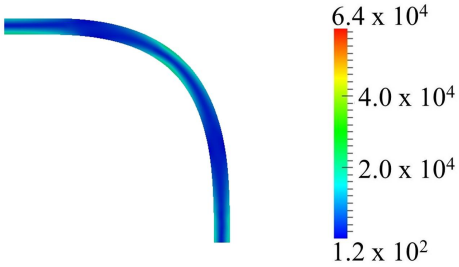
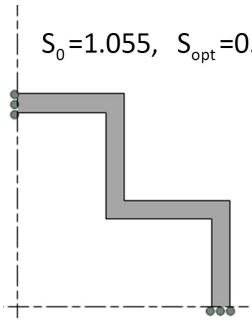	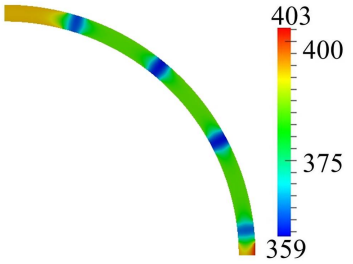	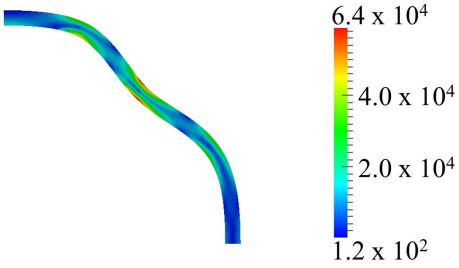

Maximized Reduced-Order Model Accuracy for Inverse Problem Applications:

Although generally applicable, the following discussion of an approach to create optimally accurate physics-based reduced-order models (ROM) is presented within the context of steady-state harmonic solid mechanics of heterogeneous solids with a range of potential material parameters. Assuming that the solid considered is excited harmonically to a steady-state in the linear elastic range, and therefore the system variables vary harmonically in time with angular frequency ω, and neglecting body forces, the governing equations and boundary conditions (i.e., boundary value problem) from conservation of momentum can be written as:

$$\begin{aligned}
&\nabla \cdot \boldsymbol{\sigma}(\vec{x},\omega) + \omega^2 \rho(\vec{x}) \vec{u}(\vec{x},\omega) = 0, \quad \forall \vec{x} \in \Omega, \\
&\boldsymbol{\sigma}(\vec{x},\omega) \cdot \vec{n}(\vec{x}) = \vec{T}(\vec{x},\omega), \quad \forall \vec{x} \in \Gamma_T, \\
&\vec{u}(\vec{x},\omega) = \vec{u}^0(\vec{x},\omega), \quad \forall \vec{x} \in \Gamma_U, \\
&\boldsymbol{\sigma}(\vec{x},\omega) = \boldsymbol{C}^{IV} : \boldsymbol{\epsilon}(\vec{x},\omega), \\
&\boldsymbol{\epsilon}(\vec{x},\omega) = \tfrac{1}{2}\left(\nabla \vec{u}(\vec{x},\omega) + \nabla \vec{u}(\vec{x},\omega)^T\right),
\end{aligned} \tag{12}$$

where $\vec{x}$ is the spatial position vector, $\boldsymbol{\sigma}(\vec{x},\omega)$ is the stress tensor, $\rho(\vec{x})$ represents the density of the solid, $\vec{u}(\vec{x},\omega)$ is the steady-state displacement amplitude field, $\vec{T}(\vec{x},\omega)$ is the applied traction amplitude vector, $\vec{u}^0(\vec{x},\omega)$ is the applied displacement amplitude, $\boldsymbol{C}^{IV}$ is the fourth-order elasticity tensor, Ω is the domain of the solid, $\vec{n}(\vec{x})$ is the unit outward normal vector to the surface of the domain, Γ, and Γ_T and Γ_U are the portions of the domain surface where traction and displacement are applied, respectively, such that $\Gamma_T \bigcup \Gamma_U = \Gamma$ and $\Gamma_T \bigcap \Gamma_U = \varnothing$. The standard weak form Galerkin approach was employed for this work to approximate the solution of the boundary value problem described by Eqns. (12) using an arbitrary approximation function of the steady-state harmonic displacement field. As such, the weak form of the steady-state dynamic solid mechanics problem can be expressed as:

$$\int_\Omega \nabla \delta\vec{u}(\vec{x}) : \boldsymbol{\sigma}(\vec{x},\omega) d\vec{x} - \int_\Omega \omega^2 \rho(\vec{x}) \delta\vec{u}(\vec{x}) \cdot \vec{u}(\vec{x},\omega) d\vec{x} - \int_{\Gamma_T} \delta\vec{u}(\vec{x}) \cdot \vec{T}(\vec{x},\omega) d\vec{x} = 0, \tag{13}$$

where $\delta\vec{u}(\vec{x})$ is an arbitrary weight function vector (i.e., trial function vector or virtual displacement vector). Therefore, all that is necessary to complete the Galerkin approach is to substitute an approximation for the displacement field and the weight function (using the same basis for both) to obtain a discretized form and a linear system of equations for each excitation frequency. The common finite element approach would be to discretize the spatial domain into elements and use polynomial approximations within each element to discretize then assemble a system of equations. However, as is commonly known, this finite element approach (referred to as the full-order modeling approach herein) typically requires at least many thousands of degrees of freedom, even for relatively simple two-dimensional problems to accurately represent the physics of the system. Alternatively, the objective of the reduced-basis form of reduced-order modeling is to identify a basis that is optimal in some sense for representing the physics of the system under consideration with far fewer degrees of freedom than the full-order (i.e., traditional finite element) model (FOM).

The core hypothesis of the reduced-basis reduced order modeling approach considered in the present work is that a relatively small number of full-order (i.e., traditional finite element) analyses based upon different values of the input parameters of interest (material parameters herein) contain

fundamental information about the potential solution fields of the BVP and can be used to derive a low-dimensional basis that can predict the solution fields for a range of input parameters (not just the specific parameter values used to generate the set of full-order analyses) with reasonably sufficient accuracy. The POD approach was applied to derive this basis from a set of full-order analyses. POD specifically derives the low-dimensional basis such that the difference between the original full-order data and the best approximation to that data with this basis is minimized in an L_2 average sense [7]. The critical question is then how to select the set of input parameters used to create the set of full-order analyses to use for creating the POD basis. In particular, this dataset must be generated in such a way to limit the number of full-order simulations necessary to ensure sufficiently accurate generalization of the reduced-order model over the admissible range of the input parameters of interest. The problem of finding a set of snapshots to create an accurate ROM can be outlined in a general way as follows. Suppose that $F : X \to V$ is a finite element (i.e., full-order) operator that maps the space of input parameters (e.g., material properties) X to the space of displacement response fields V. The goal is to find a subset $X_n \subset X$ with $F : X_n \to V_n$ to create a POD reduced-order model operator $F_\phi(V_n) : X \to V$, such that:

$$\text{if } \; F : x \to v_1 \text{ and } \; F_\phi(V_n) : x \to v_2, \quad \text{then } \; \|v_1 - v_2\| < \epsilon, \; \forall x \in X, \text{ and } \; \forall v_1, v_2 \in V,$$

where ϵ is some acceptable error tolerance for the ROM. Extending the work in [7], the core hypothesis of the proposed adaptive snapshot generation method is that maximizing the diversity of the snapshots created within the space of the input parameters of interest will maximize the generalization of the resulting reduced-order model over that parameter space.

Given a set of n_0 input parameters sets $\{\vec{\gamma}_i\}_{i=1}^{n_0}$ and the corresponding full-order analysis response fields (i.e., snapshot), a measure of the total diversity of the i^{th} snapshot (created with input parameter set $\vec{\gamma}_i$) within the set can be calculated as:

$$R^*(\vec{\gamma}_i) = \sum_{\substack{j=1 \\ j \neq i}}^{n_0} R(\vec{\gamma}_i, \vec{\gamma}_j), \tag{14}$$

where

$$R(\vec{\gamma}_i, \vec{\gamma}_j) = \frac{(\vec{u}(\vec{x}, \vec{\gamma}_i), \vec{u}(\vec{x}, \vec{\gamma}_j))}{\|\vec{u}(\vec{x}, \vec{\gamma}_i)\|_{L_2(\Omega)} \cdot \|\vec{u}(\vec{x}, \vec{\gamma}_j)\|_{L_2(\Omega)}}. \tag{15}$$

Then, provided with the diversity metric for each snapshot in the set $\{R^*(\vec{\gamma}_i)\}_{i=1}^{n_0}$, a surrogate model approach can create an approximate mapping between the input parameters and the diversity metric. Any preferred machine learning technique can be used to generate the surrogate model, with this work using support vector regression [8, 9]. The surrogate model of the diversity $R^{SM}(\vec{\gamma})$ can then be easily minimized to estimate the optimal next set of input parameters (within the domain of the parameters X) to use with the full-order model to generate another set of snapshots that would maximize the diversity of the snapshot set as:

$$\underset{\vec{\gamma} \in X}{\text{Minimize}} \quad R^{SM}(\vec{\gamma}). \tag{16}$$

Note that since the computational cost of the surrogate model is negligible, then essentially any preferred global optimization algorithm can be used, regardless of the algorithm efficiency, with a

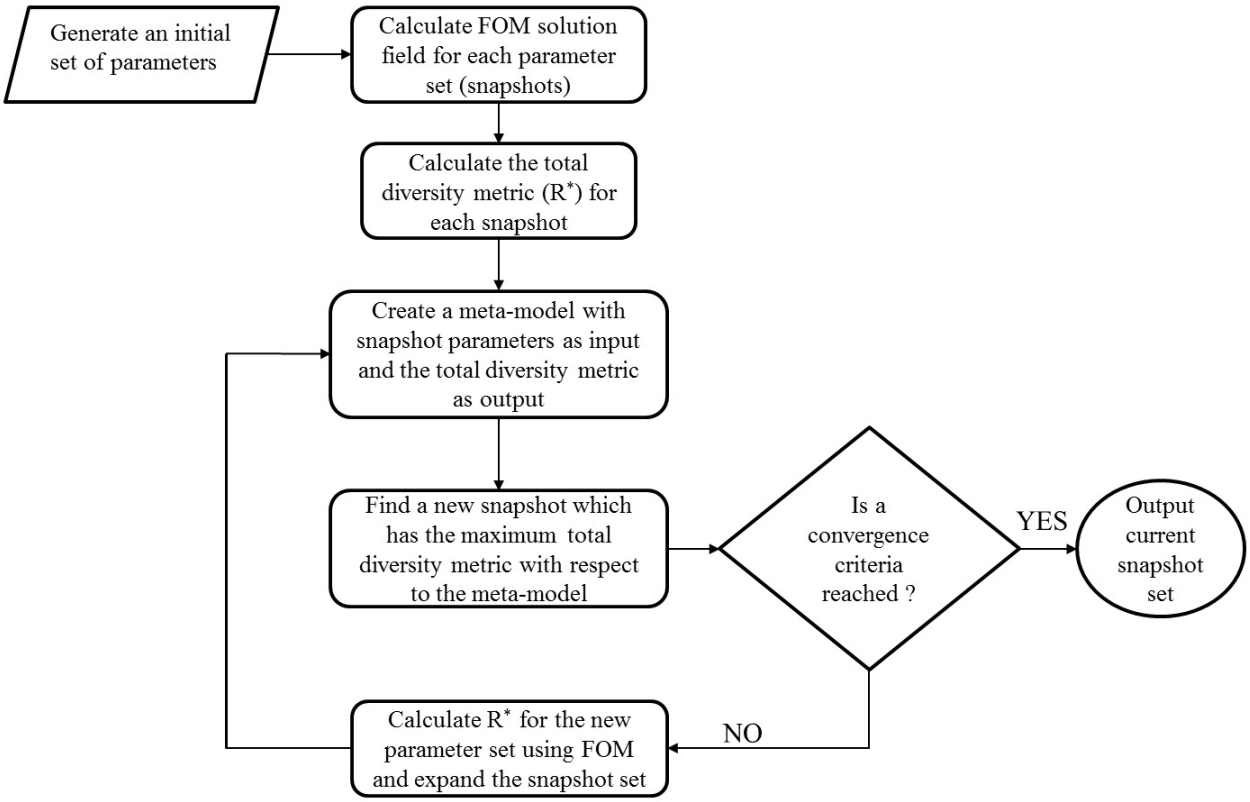

Figure 4: Flowchart describing the adaptive snapshot generation algorithm.

genetic algorithm being used for this work. Due to the expectation of some loss of accuracy in the surrogate model, an additional constraint on the parameter sets was added to the surrogate model optimization for the present work. To ensure that the input parameter sets are not overly clustered in the parameter space, the new parameter set was constrained to be a specified minimum distance δ from every other parameter set, such that:

$$\|\vec{\gamma} - \vec{\gamma}_i\| > \delta \quad \text{for } i = 1, 2, ..., n_0, \tag{17}$$

where $\|\cdot\|$ is the standard l_2-norm. Once the new set of input parameters is determined from the solution of Eqns. (16) and (17), the input parameter set is used with the full-order model to generate a new snapshot. Figure 4 shows a flowchart that describes the overall procedure for the adaptive snapshot generation algorithm to maximize snapshot diversity and resulting reduced-order model accuracy. At the completion of the snapshot generation algorithm a POD reduced-order model can be generated and utilized.

To investigate the capabilities and potential applicability of the method for adaptive generation of optimal reduced-order models, simulated case studies were considered regarding efficient and accurate modeling of the deformation of structural members with semi-localized Young's modulus distributions. The examples also examined the capabilities to then inversely characterize such material property distributions using a computational inverse solution procedure relying on this modeling. POD ROMs were generated through the adaptive approach to maximize diversity of

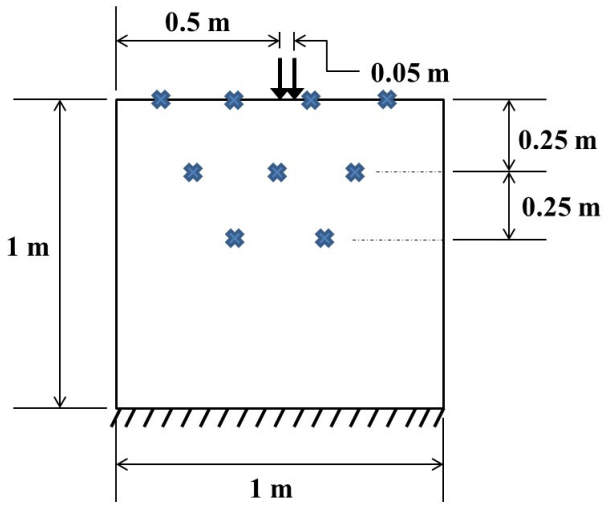

Figure 5: Schematic for NDE plate example (note that the 'x's represent the sensor locations).

the snapshot sets, and the accuracy of these ROMs was quantified with respect to full-order analysis (i.e., traditional finite element analysis) and compared to the accuracy of similar POD ROMs created from randomly generated snapshot sets. Then, the adaptively generated ROM was incorporated into an inverse characterization solution procedure. The case studies considered structures tested using frequency-response-based nondestructive testing (NDT) to then determine the material properties with nondestructive evaluation (NDE). The NDT consisted of a localized harmonic actuation applied normal to the surface of the structure at a given excitation frequency and the resulting steady-state harmonic vertical displacement amplitude was measured at a set of discrete sensor locations. One example, shown schematically in Figure 5, consisted of a $1m \times 1m \times 0.02m$ aluminum plate subject to a $1kPa$ harmonic load applied to a $5cm$ region normal to the top surface of the plate, excited to steady-state with an actuation frequency of $400Hz$. The material behavior was assumed to be linear elastic with a homogeneous density and Poison's ratio of 2700 kg/m^3 and 0.3, respectively, and the semi-localized Young's modulus distribution was assumed to be defined with a radial basis function (RBF) as:

$$E(\vec{x}) = E_0 \left[1 - \alpha \cdot exp\left(-\frac{\|\vec{x} - \vec{\zeta}\|^2}{c} \right) \right], \tag{18}$$

where E_0 is the base Young's modulus, α is the percentage of the reduction in Young's modulus, $\vec{\zeta}$ is the center of the RBF, and c is the breadth of the RBF. In other words, each Young's modulus distribution considered was parametrized by four parameters, such that $\vec{\gamma} = [\alpha, \zeta_1, \zeta_2, c]^T$. The base Young's modulus was assumed to be known as a standard nominal value for aluminum, such that $E_0 = 69GPa$.

For the adaptive snapshot generation approach, an initial random set of 10 snapshots was generated, and then the adaptive surrogate modeling approach was iteratively applied to generate the remaining snapshots in the set used to create the ROM. To examine the dependence on the total number of snapshots, snapshot sets of 10 (i.e., the original randomly generated set), 20, 30,

40, 50, and 60 were investigated, in turn. The forward modeling accuracy of the ROMs was first tested directly in comparison to the full-order modeling for 100 randomly generated parameter sets that were not included in the snapshot sets, to directly quantify the generalization capabilities of the ROMs before considering an inverse characterization problem. To test the ROM accuracy a standard relative error metric was utilized for each parameter set as follows:

$$\text{Error}(\vec{\gamma}) = \frac{\|\vec{u}^{ROM}(\vec{x},\omega,\vec{\gamma}) - \vec{u}^{FOM}(\vec{x},\omega,\vec{\gamma})\|_{\Omega}}{\|\vec{u}^{FOM}(\vec{x},\omega,\vec{\gamma})\|_{\Omega}}, \tag{19}$$

where $\vec{u}^{ROM}$ and $\vec{u}^{FOM}$ are the displacement response fields calculated with the ROM and full-order model, respectively, and $\|\cdot\|_{\Omega}$ is the chosen norm over the spatial domain, Ω, with both the L_2 and L_∞ norms being considered in the following. To provide a baseline for comparing the accuracy of the adaptively generated ROMs, ROMs were also created for the examples using an equivalent total number of randomly generated snapshots (generated in the same format as the initial set for the adaptive approach). To test the efficacy of the resulting ROMs to be used in a computational inverse problem solution procedure, each example case considered a corresponding set of tests in which the ROMs were used in an NDE procedure to estimate the stiffness parameters of the structures given simulated NDT measurements for several test cases. The inverse problem was cast as an optimization problem to determine the material parameters that minimize the relative difference between the simulated experimental NDT measurements and the response predicted by the ROM as:

$$\underset{\vec{\gamma}\in X}{\text{Minimize}} \quad \frac{\sum_{i=1}^{n_s}\left(\vec{u}^{ROM}(\vec{x_i},\omega,\vec{\gamma}) - \vec{u}^{exp}(\vec{x_i},\omega)\right)^2}{\sum_{j=1}^{n_s}\left(\vec{u}^{exp}(\vec{x_j},\omega)\right)^2}, \tag{20}$$

where again X is the domain of the unknown stiffness parameters and $\vec{u}^{exp}$ is the simulated experimental displacement responses. A standard genetic algorithm was again applied to solve the above optimization problem and identify the parameters to estimate the Young's modulus distributions, and therefore, estimate the solution to the inverse problem. The quality of the final inverse problem solution estimates were quantified through the relative L_2-error between the Young's modulus distribution defined by the parameters used to create the simulated experimental data and that estimated by the inverse characterization results as:

$$\frac{\left(\int_{\Omega}\left(E(\vec{x},\vec{\gamma}^{exp}) - E(\vec{x},\vec{\gamma}^{inv})\right)^2 d\vec{x}\right)^{1/2}}{\left(\int_{\Omega}\left(E(\vec{x},\vec{\gamma}^{exp})\right)^2 d\vec{x}\right)^{1/2}}, \tag{21}$$

where $\vec{\gamma}^{exp}$ are the parameters used to create the simulated experimental measurement data and $\vec{\gamma}^{inv}$ are the corresponding inverse solution estimates.

Figure 6 shows the average and standard deviation of the relative ROM error for the 100 test cases for both the adaptively generated ROMs and the randomly generated ROMs. As would be expected, for both approaches, the average error as well as the standard deviation of the error for the resulting ROM decreased as the number of snapshots used to construct the ROM increased. More interestingly, the ROM error corresponding to the adaptively generated snapshots was substantially lower than the the ROM error corresponding to the randomly generated snapshots by approximately a factor of 2 or more for every size of the snapshot set. In addition, the standard

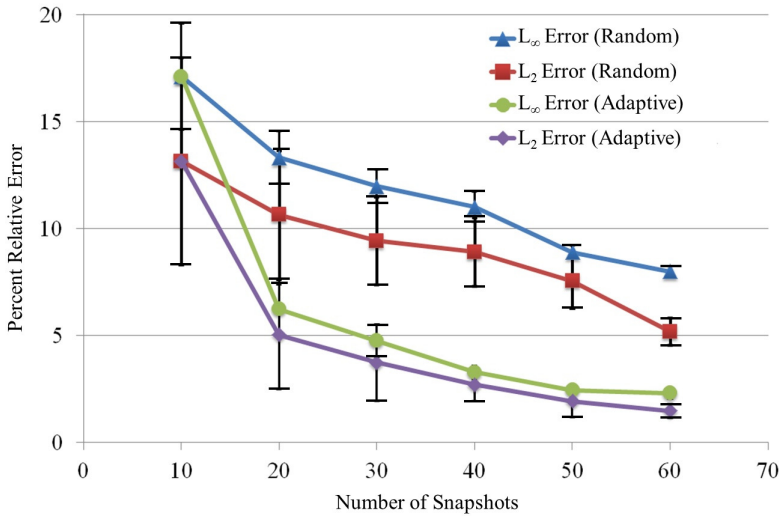

Figure 6: Average and standard deviation (error bars) with respect to the 100 test cases of the relative L_2 and L_∞ ROM errors for the randomly generated (Random) and the adaptively generated (Adaptive) ROMs for the plate example.

deviation of the error for the adaptively generated ROMs decreased considerably more quickly than the randomly generated ROMs, and while the adaptively generated ROMs appeared to have converged to some degree in terms of the error at 50 snapshots, the randomly generated ROMs show no such signs of convergence. Table 3 shows the material parameters used to create the simulated experimental measurement data for the five scenarios considered and the corresponding parameters estimated by the inverse solution process with the various ROMs (built from 20, 40, and 60 total snapshots), the respective ROM measurement error for the inverse solutions (as defined by Eqn. (20)), the respective FOM measurement error for the inverse solutions (substituting the FOM in place of the ROM in Eqn. (20)), and the error in the respective Young's modulus distributions predicted by the inverse solution estimates (as defined by Eqn. (21)). In addition, to provide further perspective on the relative accuracy of the Young's modulus distributions obtained by the inverse solution process, Figure 7 shows (as a representative example) the target (i.e., simulated experimental) Young's modulus distribution for a material property scenario compared to the Young's modulus distribution that was inversely estimated using the ROM built from 60 adaptively generated snapshots. Overall, the optimization process was able to sufficiently match the ROM response to the measurement data. More importantly, the FOM responses with the inverse solution estimates also sufficiently matched the measurement data, even though the optimization was performed with the ROM. Moreover, the FOM measurement error was minimally higher than the ROM measurement error. In other words, the inverse problem solution estimates obtained with the ROMs were nearly as accurate with respect to the FOM in terms of the measurement data, and were still within an error range in terms of the FOM to be considered an inverse problem solution estimate. As would be expected, corresponding to the accuracy in the measurement error, the resulting estimates of the Young's modulus distributions were accurate for all three ROMs, with Young's modulus reconstruction errors of less than 1% for every test.

Table 3: Target (i.e., simulated experimental) values for the RBF amplitude (α), the breadth of the RBF (c_1), and the horizontal and vertical locations of the center of the RBF (ζ_1, ζ_2) defining the Young's modulus distribution, the corresponding parameters estimated with the inverse characterization process using the ROMs created with 20 (ROM-20), 40 (ROM-40), and 60 (ROM-60) adaptively generated snapshots, and the respective ROM measurement error (M_E), the FOM measurement error (F_E), and the error in the predicted Young's modulus distribution (Y_E) for five test cases (i.e., damage scenarios) for the plate example.

		α	ζ_1	ζ_2	c	$M_E(\%)$	$F_E(\%)$	$Y_E(\%)$
Test 1	Target	0.701	0.592	0.511	0.004			
	ROM-20	0.544	0.652	0.481	0.003	2.78	3.45	0.37
	ROM-40	0.552	0.610	0.536	0.005	1.53	1.86	0.01
	ROM-60	0.552	0.607	0.521	0.005	1.45	1.57	0.01
Test 2	Target	0.416	0.841	0.832	0.002			
	ROM-20	0.310	0.763	0.782	0.003	0.72	3.12	0.04
	ROM-40	0.384	0.803	0.791	0.002	0.52	2.73	0.02
	ROM-60	0.405	0.824	0.801	0.002	0.49	1.67	0.07
Test 3	Target	0.540	0.869	0.264	0.003			
	ROM-20	0.407	0.781	0.396	0.005	5.61	4.82	0.32
	ROM-40	0.601	0.855	0.202	0.001	3.52	2.67	0.13
	ROM-60	0.451	0.860	0.236	0.003	1.46	2.22	0.08
Test 4	Target	0.639	0.544	0.647	0.005			
	ROM-20	0.558	0.598	0.607	0.003	2.89	5.14	0.48
	ROM-40	0.583	0.576	0.683	0.004	2.4	2.39	0.27
	ROM-60	0.608	0.532	0.651	0.004	2.11	1.5	0.24
Test 5	Target	0.066	0.404	0.448	0.007			
	ROM-20	0.048	0.488	0.337	0.005	0.65	4.93	0.07
	ROM-40	0.071	0.381	0.411	0.005	0.48	3.01	0.03
	ROM-60	0.061	0.414	0.491	0.006	0.46	2.47	0.03

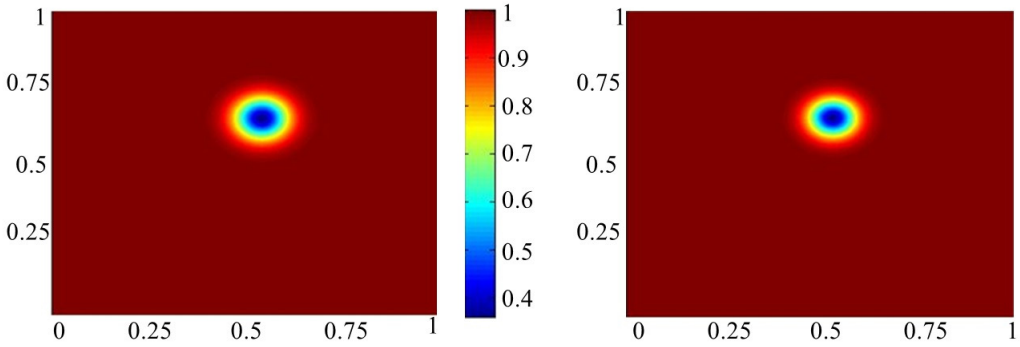

Figure 7: Spatial distribution of the Young's modulus from (a) the target (simulated experiment) and (b) the inverse characterization estimate with the ROM built from 60 adaptively generated snapshots for the fourth test scenario for the plate example.

Inverse Material Characterization Using Gappy POD with Direct Inversion:

The Gappy POD process starts by following the standard POD procedure to obtain a set of orthogonal modes from a given set of snapshots. The point in which Gappy POD diverges from standard POD is how those modes are utilized. If the full distribution (specifically, full spatial distribution for the cases herein) of a field is available, the modal coefficients (a_i) needed to reconstruct that field with the POD modes can be easily obtained by projecting the modes onto the field as:

$$a_i = \int_\Omega \vec{u}\left(\vec{\xi}\right) \cdot \vec{\phi}_i\left(\vec{\xi}\right) d\vec{\xi}. \tag{22}$$

However, projection is no longer applicable to determine the values of the modal coefficients to reconstruct the field if the entire spatial distribution is not available. Thus, the objective of Gappy POD is to provide a means to reconstruct the full spatial distribution of a field using the POD modes, but with only a partial spatial distribution of the field given. Defining $\hat{\vec{u}}(\vec{x})$ as the given partial distribution of the field of interest such that $\hat{\vec{u}}(\vec{x})$ is (incorrectly) 0 anywhere data is unavailable, then $\hat{\vec{u}}(\vec{x})$ can be expressed in terms of the corresponding, but unknown, full spatial distribution as:

$$\hat{\vec{u}}(\vec{x}) = \beta(\vec{x}, \vec{u})\, \vec{u}(\vec{x}), \tag{23}$$

where $\beta(\vec{x}, \vec{u})$ is a mask function that is defined as 0 where data is unavailable and 1 where data is available. Assuming that the full spatial distribution can be approximated with the POD modes, an approximation of $\hat{\vec{u}}(\vec{x})$ can be written in terms of the POD modes as:

$$\hat{\vec{u}}^*(\vec{x}) = \beta(\vec{x}, \vec{u}) \sum_{i=1}^{m} a_i \vec{\phi}_i(\vec{x}). \tag{24}$$

Then, based upon a least-squares criteria, the optimal set of modal coefficients to reconstruct the full spatial distribution of the field can be defined as that which minimizes an error function of the

form:

$$\varepsilon = \int_{\Omega} \left[\beta\left(\vec{x}, \vec{u}\right) \vec{u}\left(\vec{x}\right) - \beta\left(\vec{x}, \vec{u}\right) \sum_{i=1}^{m} a_i \vec{\phi}_i(\vec{x}) \right]^2 d\vec{x}. \tag{25}$$

Lastly, applying the necessary condition for extrema of a function by setting the derivative of the error function with respect to the modal coefficients to zero, the optimal set of modal coefficients, {a}, to reconstruct the full spatial distribution of the field can be determined from the solution of:

$$[M]\{a\} = \{f\}, \tag{26}$$

where

$$M_{ij} = \int_{\Omega} \beta\left(\vec{x}, \vec{u}\right) \vec{\phi}_i(\vec{x}) \cdot \vec{\phi}_j(\vec{x}) \; d\vec{x}. \tag{27}$$

and

$$f_i = \int_{\Omega} \beta\left(\vec{x}, \vec{u}\right) \vec{u}(\vec{x}) \cdot \vec{\phi}_i(\vec{x}) \; d\vec{x}. \tag{28}$$

Although potentially applicable to a variety of different physical systems, the application of the present work is characterization of the elastic modulus distribution of a solid from displacement measurements (full-field displacement response once Gappy POD has been utilized). Furthermore, the following formulation is presented with respect to a steady-state dynamic testing procedure (as could be applicable to frequency response function-based evaluation), but could easily be converted to a static problem by simply setting the excitation frequency to zero. Therefore, the forward problem and weak form defined above in Eqns. (12) and (13) are still applicable. Applying the standard finite element procedure and converting to Voigt notation, the domain can be discretized into a collection of elements, and the displacement and virtual displacement fields and their corresponding strain vectors can be approximated as:

$$\vec{u}(\vec{x}, \omega) \approx [N_{\vec{u}}(\vec{x})]\{\vec{u}^e(\omega)\}, \tag{29}$$

$$\delta\vec{u}(\vec{x}) \approx [N_{\vec{u}}(\vec{x})]\{\delta\vec{u}^e\}, \tag{30}$$

$$\{\varepsilon(\vec{x}, \omega)\} \approx [B_{\vec{u}}(\vec{x})]\{\vec{u}^e(\omega)\}, \tag{31}$$

and

$$\{\delta\varepsilon(\vec{x})\} \approx [B_{\vec{u}}(\vec{x})]\{\delta\vec{u}^e\}, \tag{32}$$

where $[N_{\vec{u}}(\vec{x})]$ is the standard matrix of shape functions for displacement interpolation and $[B_{\vec{u}}(\vec{x})]$ is the matrix of shape function spatial derivatives for strain interpolation. Substituting these field approximations into Eqn. (13), eliminating the arbitrary virtual response field vector, and assembling individual element contributions, the final finite element equations are depicted as:

$$[K]\{u\} - [M]\{u\} = \{P\}, \tag{33}$$

where

$$[K] = \sum_{element} \int_{\Omega^e} [B_{\vec{u}}(\vec{x})]^T [D][B_{\vec{u}}(\vec{x})] \; d\vec{x}, \tag{34}$$

$$[M] = \sum_{element} \int_{\Omega^e} \rho(\vec{x})\omega^2 [N_{\vec{u}}(\vec{x})]^T [N_{\vec{u}}(\vec{x})] \; d\vec{x}, \tag{35}$$

$$\{P\} = \sum_{element} \int_{\Gamma^e_{\vec{T}}} [N_{\vec{u}}(\vec{x})]^T \vec{T}(\vec{x},\omega) \; d\vec{x}, \tag{36}$$

and $[D]$ is elasticity matrix, such that:

$$\{\sigma(\vec{x},\omega)\} = [D]\{\varepsilon(\vec{x},\omega)\} \tag{37}$$

The summation over elements refers to the assembly process.

With the objective of the inverse problem being characterization of the elastic modulus distribution provided with the entire displacement field everywhere in the domain, the first step in the inverse solution formulation is to separate the elastic modulus ($E(\vec{x})$) from the elasticity matrix as:

$$[D] = [D_I]E(\vec{x}), \tag{38}$$

where D_I is now only a function of Poisson's ratio (ν). Applying the same general weak form procedure as was done previously for displacement, but now for the elastic modulus, the inverse problem weak form for the steady-state dynamic boundary value problem can be written as:

$$\begin{aligned} \int_{\Omega} \nabla \delta\vec{E}(\vec{x}) : \boldsymbol{\sigma}_I(\vec{x},\omega) E(\vec{x}) \; d\vec{x} = \int_{\Omega} \rho(\vec{x})\omega^2 \delta\vec{E}(\vec{x}) \cdot \vec{u}(\vec{x},\omega) \; d\vec{x} + \\ \int_{\Gamma_{\vec{T}}} \delta\vec{E}(\vec{x}) \cdot \vec{T}(\vec{x},\omega) \; d\vec{x}, \end{aligned} \tag{39}$$

where

$$\{\sigma_I(\vec{x},\omega)\} = [D_I]\{\varepsilon(\vec{x},\omega)\}, \tag{40}$$

and $\delta\vec{E}$ is the virtual elastic modulus vector (matching the dimension of the displacement field, and therefore, the number of equilibrium equations, even though the modulus itself is a scalar). Now discretizing the domain into finite elements to represent the elastic modulus and again using Voigt notation where applicable, the elastic modulus and virtual elastic modulus vector and their corresponding gradients can be approximated as:

$$E(\vec{x}) \approx [N_E(\vec{x})]\{E^e\}, \tag{41}$$

$$\delta\vec{E}(\vec{x}) \approx [N_{\delta\vec{E}}(\vec{x})]\{\delta\vec{E}^e\}, \tag{42}$$

$$\{\nabla E(\vec{x})\} \approx [B_E(\vec{x})]\{E^e\}, \tag{43}$$

and

$$\{\nabla \delta\vec{E}(\vec{x})\} \approx [B_{\delta\vec{E}}(\vec{x})]\{\delta\vec{E}^e\}, \tag{44}$$

where $[N_E(\vec{x})]$ is now the matrix of shape functions for elastic modulus interpolation, $[N_{\delta\vec{E}}(\vec{x})]$ is the expanded version (to match the dimensions of the displacement) of the matrix of shape functions for elastic modulus interpolation, and $[B_E(\vec{x})]$ and $[B_{\delta\vec{E}}(\vec{x})]$ are the respective matrices

of these shape function spatial derivatives. Substituting these field approximations as well as the previously-defined discretization of the given displacement field into Eqn. (39), eliminating the arbitrary virtual elastic modulus field vector, and assembling individual element contributions, the final finite element equations for the direct inversion elastography problem are depicted as:

$$[K_I]\{E\} = \{P_I\} + [M_I]\{u\}, \tag{45}$$

where

$$[K_I] = \sum_{element} \int_{\Omega^e} [B_{\delta\vec{E}}(\vec{x})]^T [D_I][B_{\vec{u}}(\vec{x})]\{\vec{u}^e\}[N_E(\vec{x})]\ d\vec{x}, \tag{46}$$

$$[M_I] = \sum_{element} \int_{\Omega^e} \rho(\vec{x})\omega^2 [N_{\delta\vec{E}}(\vec{x})]^T [N_{\vec{u}}(\vec{x})]\ d\vec{x}, \tag{47}$$

and

$$\{P_I\} = \sum_{element} \int_{\Gamma^e_{\vec{T}}} [N_{\delta\vec{E}}(\vec{x})]^T \vec{T}(\vec{x},\omega)\ d\vec{x}. \tag{48}$$

Since $[K_I]$ is typically non-square and Eqn. (45) is typically an overdetermined system ($[K_I]$ has dimensions $3N \times N$, where N is the number of nodes in the mesh if the same mesh is used for both fields), the elastic modulus cannot be estimated by simply inverting $[K_I]$. Thus, as is common, a least-squares approach was used here to solve Eqn. (45) for $\{E\}$. As such, the nodal values of elastic modulus can be determined as:

$$\{E\} = \left([K_I]^T[K_I]\right)^{-1} [K_I]^T \left(\{P_I\} + [M_I]\{u\}\right). \tag{49}$$

The overall algorithm for direct inversion of a material property distribution from partial-field response measurements with Gappy POD can be summarized as follows:

Given: The geometry of the structure of interest, the boundary conditions and partial-field response measurements from a nondestructive testing procedure, and any available material properties.

Find: The unknown material property distribution.

Step 1: Generate (e.g., randomly or through some other sampling procedure) a set of potential distributions for the unknown material property, using any information available *a priori* relating to the likely nature of the unknown distribution, and use a forward analysis procedure to produce the corresponding full-field structural responses for each property distribution from the nondestructive testing conditions.

Step 2: Calculate the POD modes from the set of full-field structural responses, and select the modes (based on a user-defined criteria, such as the eigenvalue energy) to be retained for Gappy POD field reconstruction.

Step 3: Reconstruct the full-field structural response from the given partial-field measurements with Gappy POD.

Step 4: Calculate an estimate to the unknown material property distribution using the direct inversion procedure with the reconstructed full-field structural response and nondestructive test boundary conditions.

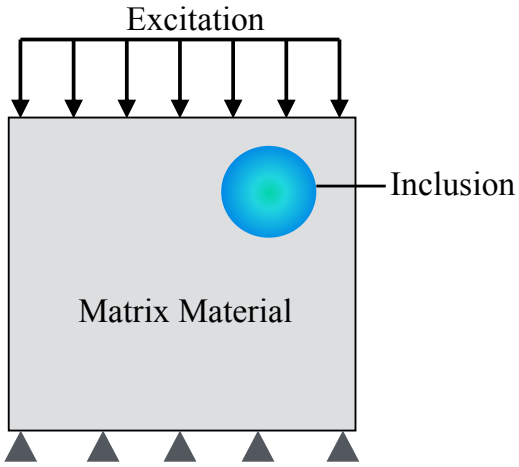

Figure 8: Schematic for the numerically simulated examples representing characterization of an elastic modulus distribution with an inclusion.

Examples were considered and evaluated to examine the potential benefits and capabilities of using the direct inversion approach with Gappy POD to characterize the elastic modulus distribution in solids from partial-field measurements. Numerically simulated experiments were based upon characterization of elastic modulus distributions with circular inclusions (hard or soft), as shown schematically in Figure 8. Again, a Gaussian radial basis function representation was chosen to define the localized elastic modulus variations, as defined in Eqn. (18). For the inverse characterization process, it was assumed to be known *a priori* that the variation in elastic modulus was similarly localized in nature (of course, with the size, amplitude, and location of this variation to be estimated by characterizing the entire spatial distribution of the elastic modulus with the direct inversion procedure). Therefore, the process to create the POD modes used snapshots generated with this same RBF parameterization of the elastic modulus distribution. For one example, a soft material block was modeled as a 50 $mm \times 50$ mm square domain with the bottom fixed to a rigid support that was expected to have a hard inclusion. The entire material (matrix and inclusion) was assumed to be known to be nearly incompressible, and a Poisson's ratio of 0.49999 was assigned. A simulated static test was implemented by applying a 0.2 N/mm (factoring out the arbitrary thickness) excitation uniformly to the top surface of the block. Then, the static vertical displacement response to the loading was measured at 100 uniformly spaced discrete locations, as shown in Figure 9. 5% Gaussian white noise was added to the measurements for this first example, which was deemed to be reasonable level of noise that could be expected from similar tests (note that this level of noise is commensurate with the highest levels of noise used in prior referenced works on direct inversion strategies with full-field response measurements).

For the process of generating the snapshots for POD, the elastic modulus of the background material (i.e., matrix material) was assumed to be fixed at 15 kPa. Alternatively, the parameters defining the inclusion based on the RBF description were assumed to be variable. The specific parameter values used to create the snapshots were chosen arbitrarily by uniformly sampling the space of the four variable parameters (the two spatial coordinates, amplitude, and breadth). Three

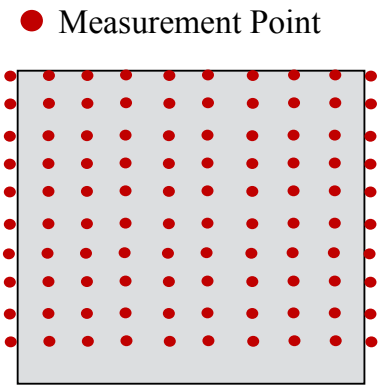

Figure 9: Schematic of the vertical displacement sensor locations (red dots) for the example soft matrix with a hard inclusion.

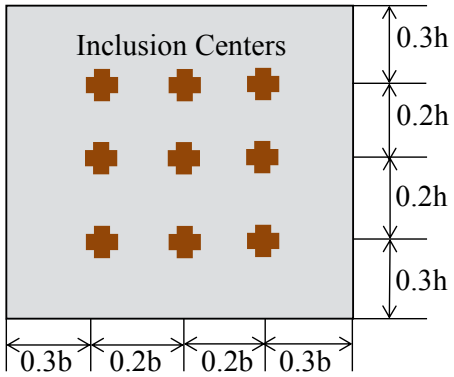

Figure 10: Schematic of the nine inclusion centers used separately to generate the snapshots for POD for the numerically simulated examples.

values were chosen for each spatial coordinate of the inclusion center and two values were chosen each for the amplitude and breadth of the inclusion, and one last scenario with no inclusion (i.e., homogeneous matrix material) was added, for a total of 37 parameter combinations used to create snapshots. Figure 10 shows the nine location combinations of the inclusion center used to generate the snapshots. The values of the other two parameters used to create the parameter combinations were chosen based on an expectation of what the lower and upper-end would be for the application, using 1 and 3 for the amplitude parameter (i.e., modulus at inclusion center of 30 kPa and 60 kPa) and 5 mm and 15 mm for the breadth parameter.

Figure 11 shows a representative example trial of a simulated displacement response field from a randomly generated parameter set and including the 5% Gaussian white noise in comparison to the displacement response field reconstructed from the 100 response measurements of that response field with the Gappy POD procedure. In general, the Gappy POD reconstruction of the displacement response from partial-field measurements was found to be accurate, producing response distributions that were nearly identical to the full simulated responses, with errors consistent with the example shown, which had relative L_2 and L_∞ errors in the displacement reconstruction of 7.4%

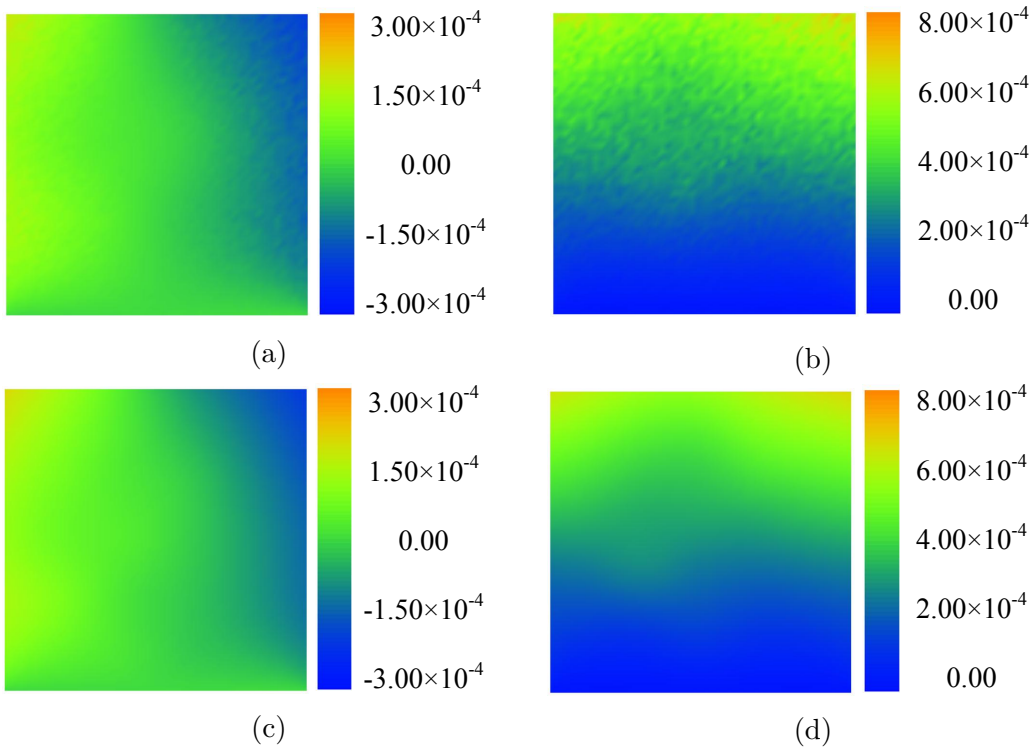

Figure 11: Representative example of the (a) horizontal and (b) vertical components of a simulated experimental displacement field with 5% Gaussian white noise and the (c) horizontal and (d) vertical components of the corresponding reconstructed displacement field from Gappy POD with only the discrete measurement data (color contours in units of m) for the example soft matrix with a hard inclusion.

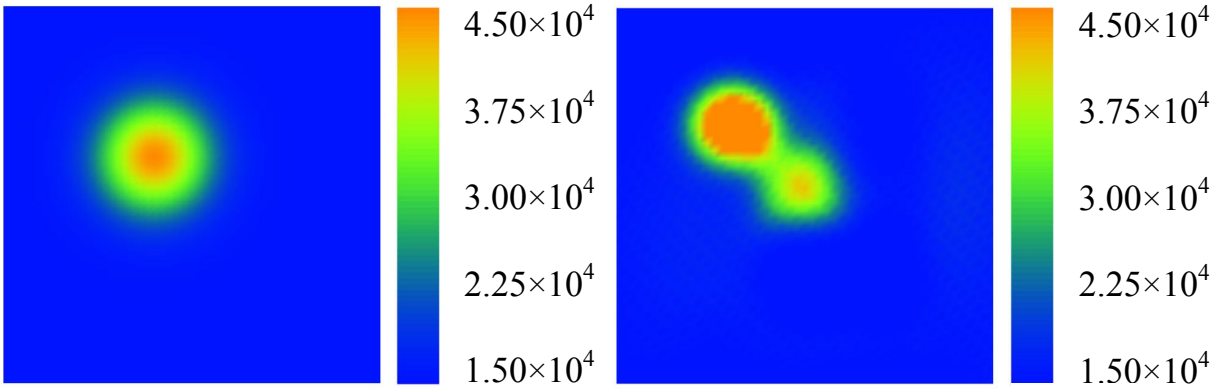

Figure 12: Representative example of (a) the elastic modulus distribution used to simulate experimental measurements (i.e., the target modulus distribution) and (b) the corresponding elastic modulus distribution estimated with the direct inversion approach with Gappy POD full-field displacement reconstruction from the partial-field measurements (color contours in units of Pa) for the example soft matrix with a hard inclusion.

and 18.5%, respectively. More importantly, Figure 12 shows a representative example of an elastic modulus distribution used to generate simulated experimental measurements (i.e., target modulus distribution) and the corresponding elastic modulus distribution estimated by the direct inversion procedure with Gappy POD displacement reconstruction. There was a noticeable amount of error in the modulus reconstruction, and the relative L_2 and L_∞ errors in the modulus estimation compared to the target distribution were 21% and 43%, respectively. However, the localization of the modulus distribution was accurate, indicating a single harder region within the solid, and the matrix modulus value and the maximum inclusion modulus value were nearly identical to the target distribution. Again, it should be noted that the direct inversion process does not restrict the distribution of the modulus to be localized, which emphasizes the significance of having recovered the correct localization with the inversion procedure. Moreover, the accuracy of the modulus reconstruction was commensurate, if not qualitatively better, than in alternate works in the literature on direct inversion techniques [10, 11], with those approaches using full-field response measurements, rather than the partial-field measurements used here. To further expand on the benefits of the direct inversion with Gappy POD, Figure 13 shows the elastic modulus distribution estimated by the direct inversion procedure with the original simulated full-field displacement with the added 5% Gaussian white noise. Clearly, the direct inversion procedure applied to the noisy data was unable to remotely come close to estimating the target elastic modulus distribution, indicating the significance of the noise filtering capability of the Gappy POD field reconstruction prior to direct inversion. For all test cases investigated the Gappy POD with direct inversion procedure was able to reconstruct the full-field displacement and then estimate the elastic modulus distribution with an accuracy consistent with the representative example shown. In particular, the capability of the Gappy POD with direct inversion procedure to correctly localize and accurately estimate the magnitude of the elastic modulus distribution remained consistent.

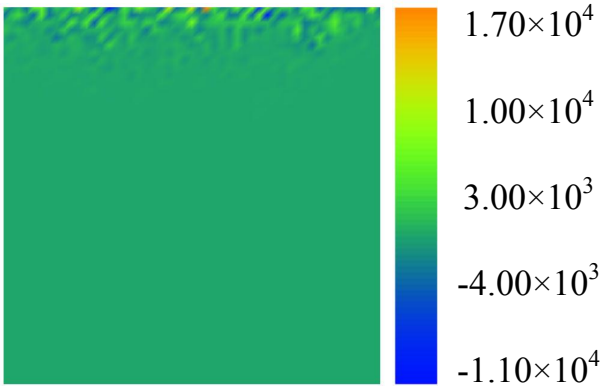

Figure 13: Example of an elastic modulus distribution estimated with the direct inversion approach applied directly to the full-field simulated experimental data with noise (i.e., without using Gappy POD) (color contours in units of Pa) for the example soft matrix with a hard inclusion.

Multi-Objective Optimization for Computationally Efficient Nondestructive Evaluation:

This portion of the work also focused on NDE of solid continua and utilized the common approach of casting the inverse characterization problem as an optimization problem to determine the unknown parameters of the structure to minimize the difference between the measured response and those predicted by a numerical representation of the structure (e.g., finite element or boundary element analysis) subject to the nondestructive testing conditions. This type of optimization strategy to approximate the solution of inverse characterization problems provides several benefits, including the capability to address a variety of physical processes/measurements, even simultaneously, and providing quantitative results. However, there are also inherent challenges in addition to the ubiquitous ill-posedness associated with inverse problems, most prevalent being the large computational expense of this optimization approach. The key to using multi-objective optimization for these inverse problems is as simple as dividing up the measurement components or spatial distribution into several separate objective functionals to be minimized simultaneously, but separately, which could be viewed as (e.g., for the case of dividing the spatial distribution of the measurements):

$$\underset{\vec{\alpha}}{\text{Minimize}} \begin{cases} \|\vec{R}^{sim}(\vec{\alpha},\vec{x}) - \vec{R}^{exp}(\vec{x})\|_{\Gamma_1} \\ \|\vec{R}^{sim}(\vec{\alpha},\vec{x}) - \vec{R}^{exp}(\vec{x})\|_{\Gamma_2} \\ \vdots \\ \|\vec{R}^{sim}(\vec{\alpha},\vec{x}) - \vec{R}^{exp}(\vec{x})\|_{\Gamma_n} \end{cases}, \tag{50}$$

where $\vec{\alpha}$ is the vector of parameters to be determined to characterize the desired structural properties, $\vec{R}^{sim}$ is the simulated response field to estimate the NDT response for a given set of parameters, $\vec{R}^{exp}$ is the experimentally measured response field (i.e., optimization target), $\|\cdot\|_{\Gamma}$ is some suitable metric norm with respect to the domain of the nondestructive measurements, Γ_i is the i^{th} subdivision of the domain of the response field measurements obtained from nondestructive testing and n is the total number of subdivisions. Then, any preferred multi-objective optimization algorithm can be employed to determine the Pareto front for Eqn. (50), which can be thought of as the set of

all possible solutions to the inverse problem that have a lower value for at least one of the separate objective functionals in comparison to any other solution estimate seen throughout the optimization process. This work employed a controlled elitist multi-objective genetic algorithm (CEMGA) [12, 13] to determine the Pareto front in the example cases considered therein. When the multi-objective optimization process is complete, a single solution estimate for the inverse problem can be attained through some chosen final decision criteria, such as the minimum sum of all objective functionals, such as:

$$\underset{\vec{\alpha}\in\{\vec{\alpha}_i\}_{i=1}^{p}}{\text{Minimize}} \sum_{j=1}^{n} \|\vec{R}^{sim}(\vec{\alpha},\vec{x}) - \vec{R}^{exp}(\vec{x})\|_{\Gamma_j}, \tag{51}$$

where $\{\vec{\alpha}_i\}_{i=1}^{p}$ is the set of p potential solutions identified as part of the Pareto front. Applying multi-objective optimization rather than the standard single objective optimization to inverse characterization problems was found to be a simple yet effective approach to substantially reduce the computational expense and improve the consistency of the solution accuracy for inverse characterization.

The primary feature of the multi-objective optimization that leads to improved inverse solution capabilities is that substantial diversity of the solution estimates is maintained throughout the search process by evolving a set of optima (i.e., the Pareto front) rather than a single optimum throughout an iterative optimization process. By maintaining diversity, the multi-objective optimization process is uniquely able to traverse the large parameter search spaces that are typical of inverse characterization problems efficiently and consistently, avoiding stalling and convergence to local minima. An additional benefit of the diversity in the solution estimates provided by multi-objective optimization is the resulting improvement in the ability to reveal the variety of solutions that may exist for ill-posed (particularly non-unique) problems. As a direct reason for non-uniqueness can be insufficiency of the parameterization of the properties to be determined, the solution diversity provided by multi-objective optimization can thus be assumed to be able to provide insight into the changes to the parameterization necessary to subsequently produce more unique and accurate inverse solutions. To provide additional context, the following discussion will provide example scenarios based upon the class of NDE problems relating to characterizing an unknown quantity of localized changes in properties (e.g., damage or defect characterization). However, this approach should be able to be similarly implemented for a variety of inverse characterization problems, particularly those for which some property of the unknown field is known *a priori* to be (semi-) localized in the parameter space.

The overall structure of the optimization-type NDE algorithm incorporating an adaptive self-evolving parameterization approach with multi-objective optimization is shown in Figure 14. The core hypothesis of the self-evolving parameterization component of the algorithm developed is that the distribution of solutions in the parameter space produced through multi-objective optimization provides guidance as to whether a specific physical parameter should be expanded. In the localized property characterization context, in which the primary method to expand the parameterization could be to increase the number (n) of basis functions with compact (or semi-compact) support used to define the property distribution along with their associated unknown parameters to be determined by the inversion, the self-evolving parameterization component of the characterization algorithm could be implemented as follows:

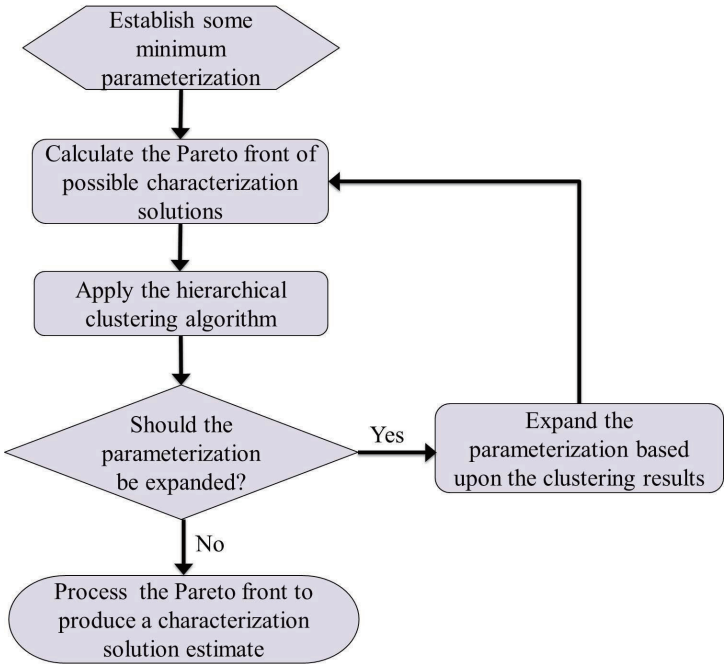

Figure 14: Flowchart of the multi-objective optimization-type NDE algorithm with adaptive self-evolving parameterization.

Given - The Pareto front of potential solutions to the inverse characterization problem (e.g., spatial coordinates of the centroid for each localized property change and any associated parameters) subject to the current value of n (i.e., the number of compactly or quasi-compactly supported basis functions used to define the localized change).

Step 1 - Identify the $n+1$ regions of localized property change whose centroids are separated by the largest Euclidean distance from the entire Pareto set of solutions (noting that each solution set could contain multiple localized property changes depending on the value of n), referred to as the $n+1$ "Parameterization Poles".

Step 2 - Identify and average all regions of localized property changes that overlap with each Parameterization Pole to produce the $n+1$ "Cluster Means" of the localized property changes.

Step 3 - Do any of the Cluster Means overlap?
Yes $\rightarrow$ STOP (do not update the parameterization further).
No $\rightarrow$ SET $n = n+1$ and GO TO Step 1.

To examine the capability of the self-evolving parameterization approach utilizing multi-objective optimization for NDE to efficiently and accurately characterize localized property changes in solid continua several simulated examples of damage characterization within structural steel plates (as could potentially be affected by erosion) were considered. More specifically, the example NDE cases sought to characterize the size and location of circular regions of material loss within the steel plates considered. Figure 15 shows a schematic for one set of test cases, which consisted of an arbitrarily thin $1\ m \times 1\ m$ square section with the bottom fixed to a rigid support. The simulated NDT consisted of applying a $1\ kN/m$ (factoring out the arbitrary thickness) harmonic excitation

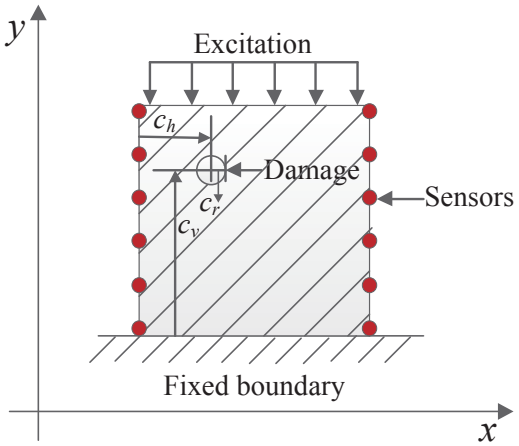

Figure 15: Schematic of the damaged square plate example.

to the top surface of the plate at an excitation frequency of 20 Hz, and then measuring the vertical and horizontal displacements at 99 equally-spaced increments along the left and right surfaces. For both generating the experimental data and simulating the forward problem during the inverse solution process the structures were assumed to behave linearly and be defined by steady-state dynamic plane stress solid mechanics, and all analyses were performed using the finite element method. The inverse problems to determine the parameters defining the damage in the example structures were cast in the form of the following multi-objective optimization problem, arbitrarily having selected to divide the displacement measurements into four groupings:

$$\min_{\vec{\alpha}} \begin{cases} \gamma_1(\vec{\alpha}) = \left(\frac{\sum_{j=1}^{n} \left(U_{1j}^{exp} - U_{1j}^{sim}(\vec{\alpha}) \right)^2}{\sum_{j=1}^{n} \left(U_{1j}^{exp} \right)^2} \right)^{1/2} \\ \gamma_2(\vec{\alpha}) = \left(\frac{\sum_{j=1}^{m} \left(U_{2j}^{exp} - U_{2j}^{sim}(\vec{\alpha}) \right)^2}{\sum_{j=1}^{m} \left(U_{2j}^{exp} \right)^2} \right)^{1/2} \\ \gamma_3(\vec{\alpha}) = \left(\frac{\sum_{j=1}^{k} \left(U_{3j}^{exp} - U_{3j}^{sim}(\vec{\alpha}) \right)^2}{\sum_{j=1}^{k} \left(U_{3j}^{exp} \right)^2} \right)^{1/2} \\ \gamma_4(\vec{\alpha}) = \left(\frac{\sum_{j=1}^{l} \left(U_{4j}^{exp} - U_{4j}^{sim}(\vec{\alpha}) \right)^2}{\sum_{j=1}^{l} \left(U_{4j}^{exp} \right)^2} \right)^{1/2} \end{cases}, \tag{52}$$

where $\vec{\alpha}$ is the vector containing the parameters of the unknown damage to be determined in the inverse problem, U_{1j}^{exp}, U_{2j}^{exp}, U_{3j}^{exp} and U_{4j}^{exp} are the experimentally measured displacement at the j^{th} measurement location in the four groupings, and U_{1j}^{sim}, U_{2j}^{sim}, U_{3j}^{sim} and U_{4j}^{sim} are the numerically simulated displacement at the j^{th} measurement location in the four groupings. The four objective functions for this example were simply defined by dividing the measurements with respect to the two sides and the two directional components.

One of the simulated scenarios to test the capabilities of the NDE algorithm with self-evolving parameterization was a case with two actual damage regions in the simulated experiment. Figure 16 shows a representative example from five trials of the inverse solution process of the Pareto front solution estimates and Figure 17 shows the corresponding measurement error for the four

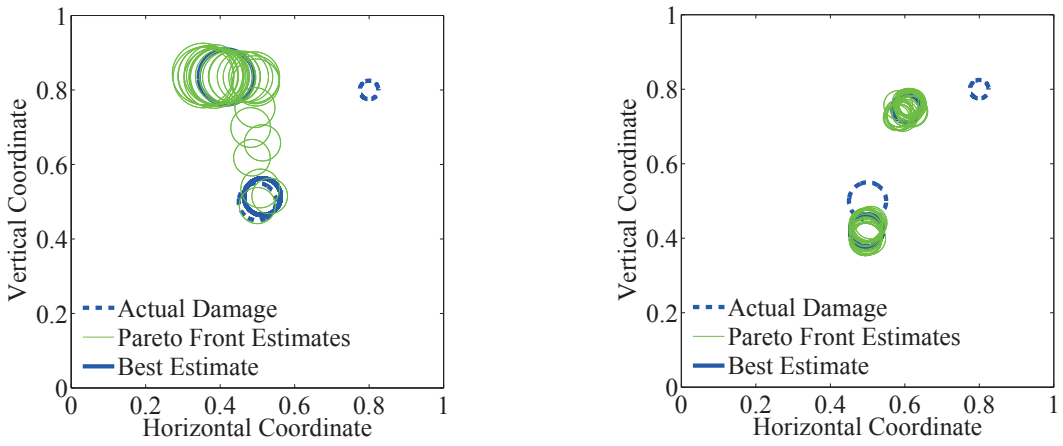

(a) (b)

Figure 16: Representative results of the Pareto front damage region solution estimates obtained from the NDE algorithm with self-evolving parameterization after (a) the first iteration with a single damage region parameterization and (b) the second iteration for which the parameterization had been automatically updated to two damage regions, along with the best individual from each Pareto front, and compared to the actual (experimental) two damage regions for the example square plate.

objectives for the "best" individual from each of the Pareto fronts at each solution iteration (as the parameterization evolved), and Figure 18 shows the final solution estimate from the converged algorithm for this example with two actual damage regions. The final solution estimates for all trials of the test cases were similarly accurate as this example shown, with both the sizes and locations of the damage regions being relatively accurate. The ability of the adaptive inverse solution process to consistently and efficiently determine the exact number of damage regions and provide relatively accurate estimations of the location and size of these damages based solely on surface measurements is significant. Moreover, the NDE algorithm with self-evolving parameterization was found to be robust to potential noise in the measurement data.

REFERENCES

[1] D. E. Goldberg, *Genetic Algorithms in Search, Optimization and Machine Learning*, 1st ed. Boston, MA, USA: Addison-Wesley Longman Publishing Co., Inc., 1989.

[2] M. Mitchell, *An Introduction to Genetic Algorithms*. Cambridge, MA, USA: MIT Press, 1998.

[3] P. Armand, J. C. Gilbert, and S. Jan-Jégou, "A feasible bfgs interior point algorithm for solving convex minimization problems," *SIAM Journal on Optimization*, vol. 11, no. 1, pp. 199–222, 2000.

[4] A. Forsgren, P. E. Gill, and M. H. Wright, "Interior methods for nonlinear optimization," *SIAM review*, vol. 44, no. 4, pp. 525–597, 2002.

[5] M. Avriel, *Nonlinear Programming: Analysis and Methods*. Courier Dover Publications, 2012.

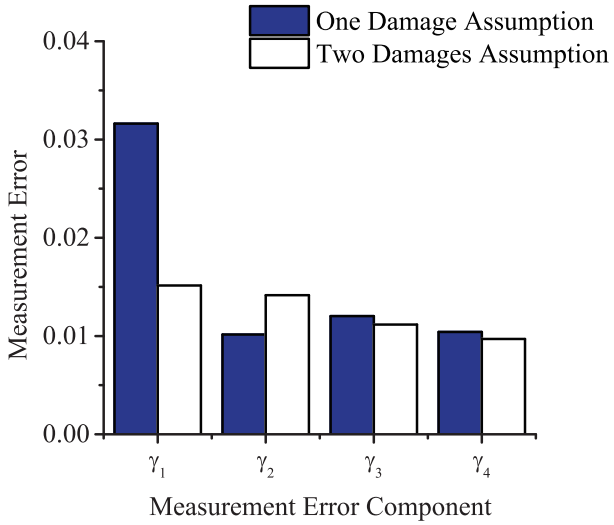

Figure 17: Measurement error for the four objectives for the (best) individual in the Pareto front damage region solution estimates obtained from the NDE algorithm with self-evolving parameterization after the first iteration with a single damage region parameterization (One Damage Assumption) and the second iteration for which the parameterization had been automatically updated to two damage regions (Two Damages Assumption) for the representative results for the example square plate.

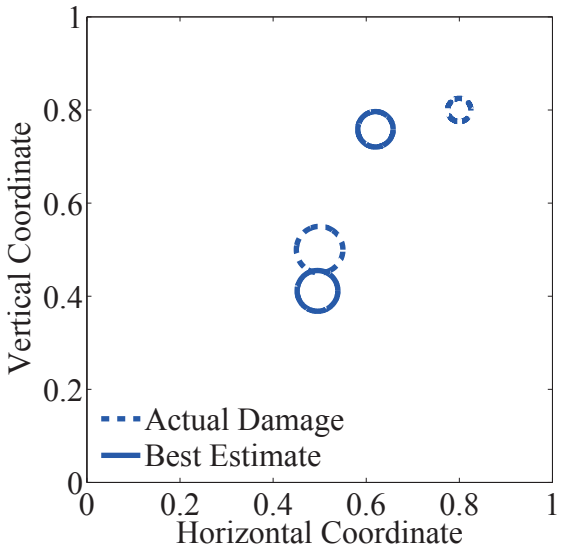

Figure 18: Final (best) solution estimate obtained from the NDE algorithm with self-evolving parameterization compared to the actual (experimental) two damage regions for the example square plate structure.

[6] A. A. Oberai, N. H. Gokhale, and G. R. Feijóo, "Solution of inverse problems in elasticity imaging using the adjoint method," *Inverse Problems*, vol. 19, no. 2, p. 297, 2003.

[7] J. C. Brigham and W. Aquino, "Inverse viscoelastic material characterization using pod reduced-order modeling in acoustic–structure interaction," *Computer Methods in Applied Mechanics and Engineering*, vol. 198, no. 9, pp. 893–903, 2009.

[8] A. J. Smola and B. Schölkopf, "A tutorial on support vector regression," *Statistics and Computing*, vol. 14, no. 3, pp. 199–222, Aug. 2004. [Online]. Available: http://dx.doi.org/10.1023/B:STCO.0000035301.49549.88

[9] S. R. Gunn, "Support vector machines for classification and regression," ISIS technical report, Tech. Rep. 14, 1998.

[10] Y. Zhu, T. Hall, and J. Jiang, "A finite-element approach for young's modulus reconstruction," *Medical Imaging, IEEE Transactions on*, vol. 22, no. 7, pp. 890–901, July 2003.

[11] E. Park and A. M. Maniatty, "Shear modulus reconstruction in dynamic elastography: time harmonic case," *Physics in Medicine and Biology*, 2006.

[12] K. Deb and D. Kalyanmoy, *Multi-Objective Optimization Using Evolutionary Algorithms*. New York, NY, USA: John Wiley & Sons, Inc., 2001.

[13] K. Deb, A. Pratap, S. Agarwal, and T. Meyarivan, "A fast and elitist multiobjective genetic algorithm: Nsga-ii," *Trans. Evol. Comp*, vol. 6, no. 2, pp. 182–197, Apr. 2002. [Online]. Available: http://dx.doi.org/10.1109/4235.996017